J. Fluid Mech. (2013), *vol.* 733, *pp.* 189–220.
doi:10.1017/jfm.2013.436

Optimal control of dissimilar heat and momentum transfer in a fully developed turbulent channel flow

A. Yamamoto[1], Y. Hasegawa[2,†] and N. Kasagi[3]

[1]Toshiba Corporation Power Systems Company, 2-4, Suehiro-Cho Tsurumi-Ku, Yokohama 230-0045, Japan

[2]Institute of Industrial Science, The University of Tokyo, Komaba 4-6-1, Meguro-ku, Tokyo 153-8505, Japan

[3]Center of Research and Development Strategy, Japan Science and Technology Agency, K's Gobancyo, 7, Gobancho Chiyoda-ku, Tokyo 102-0076, Japan

(Received 12 November 2012; revised 2 July 2013; accepted 16 August 2013; first published online 23 September 2013)

Sustained friction drag reduction and heat transfer augmentation are simultaneously achieved in a fully developed channel flow where the averaged transport equations and wall boundary conditions for momentum and heat have identical form. Zero-net-mass-flux wall blowing and suction is assumed as a control input and its spatio-temporal distribution is determined based on optimal control theory. When the root-mean-square value of the control input is 5 % of the bulk mean velocity, the friction drag is decreased by 24 % from the uncontrolled value, whereas the heat transfer is more than doubled. Optimizations with different amplitudes of the control input and different Reynolds numbers reveal that the optimal control inputs commonly exhibit the property of a downstream travelling wave, whose wavelength is $\sim$250 in wall units and phase velocity is $\sim$30 % of the bulk mean velocity. Detailed analyses of the controlled velocity and thermal fields show that the travelling wave input contributes to dissimilar heat transfer enhancement through two distinct mechanisms, i.e. direct modification of the coherent velocity and thermal fields and an indirect effect on the random fields. The present results show that the divergence-free velocity vector and the conservative scalar are essentially different, and this is a key to achieving dissimilar heat transfer enhancement in turbulent shear flows.

Key words: control theory, drag reduction, mixing enhancement

1. Introduction

Considering that modern society is built on the interconversion between heat and mechanical/electric energy, smart handling of heat and fluid flow is a key technology toward realizing a future sustainable society. For example, the performance of heat exchangers has significant impact on the overall efficiency of heat engines such as regenerative gas turbines, whereas turbine blade cooling technology is crucial for increasing the turbine inlet temperature. Recently, heat transfer enhancement

† Email address for correspondence: ysk@iis.u-tokyo.ac.jp

techniques have also attracted much attention in the efficient use of low/medium-temperature heat sources such as exhaust heat of internal combustion engines and power plants as well as geothermal energy.

In order to drive fluid through a flow passage in energy devices, a pressure gradient is generally imposed along the streamwise direction so as to overcome the drag acting at fluid–solid boundaries. The applied pumping power has to be minimized, since it is eventually converted to heat by the fluid viscosity, and therefore causes entropy generation.

In real applications, the objectives in designing heat exchangers are quite broad, namely minimizing weight, volume, heat transfer surface, and frontal area to name a few. In addition, there often exist a number of different constraints such as required overall heat transfer, maximum pressure drop, maximum height, width or length of a heat exchanger. Consequently, the relative cost and merit of the pressure drop and heat transfer strongly depend on the specific application. For instance, in recovering exhaust heat from internal engines, a significant challenge is to reduce the total weight and volume of a heat exchanger. In such a case, enhancement of heat transfer might be more important than suppression of the pressure drop. Among various requirements mentioned above, enhancing heat transfer with diminishing pressure loss is one of the ultimate goals in heat transfer technology. However, achieving such dissimilar heat transfer enhancement could be a difficult task owing to the similarity between the transport equations of momentum and heat.

The so-called Reynolds analogy (Reynolds 1874) between momentum and scalar transfer is one of the most widely used concepts in predicting heat and mass transfer in engineering flows (see e.g. Keys, Crawford & Weigand 2005). However, its success implies a fundamental difficulty in achieving heat transfer enhancement with the friction drag reduced or not increased as much as the heat transfer. In fact, existing heat transfer enhancement techniques such as the offset strip fin (Manglik & Bergles 1995), corrugated duct (Stasiek *et al.* 1996), vortex generator (Eiamsa-ard & Promvonge 2011) and transverse rib (Nagano, Hattori & Houra 2004) are accompanied by a significant pressure loss, the rate of increase of which is usually larger than that of the heat transfer. As a result, none of those techniques improves on a flat surface in terms of heat transfer per unit pumping power. Therefore, a further breakthrough has to be made in order to establish a strategy for achieving dissimilar heat transfer enhancement.

Recently, Kasagi *et al.* (2012) re-examined the governing equations and wall boundary conditions for momentum and heat transfer in a fully developed turbulent channel flow in order to clarify possible scenarios of dissimilar control. Among these scenarios, the dissimilarity caused by a fundamental difference between the divergence-free velocity vector and the conservative scalar appears to be most promising for establishing a universal control strategy. In an incompressible fluid, the pressure field responds instantaneously so that the velocity field is projected on to the divergence-free space. Therefore, the three components of the velocity vector are coupled through the continuity constraint. On the other hand, there is no such restriction on a scalar quantity.

This inherent difference is successfully exploited by Hasegawa & Kasagi (2011) to achieve significant dissimilar heat transfer enhancement even in flows where the averaged momentum and energy transport equations have an identical form. They applied a suboptimal control theory (Lee, Kim & Choi 1998) to determine zero-net-mass-flux wall blowing and suction in a fully developed turbulent channel flow. The resultant heat transfer is enhanced by a factor of roughly three from that of the

uncontrolled flow, while the pressure drop is only doubled, when the root-mean-square (r.m.s.) value of the control input is 5 % of the bulk mean velocity. In addition, the obtained control input exhibits a travelling-wave-like property. Dissimilarity caused by such a coherent control input is of great interest, since it opens up the possibility of achieving dissimilar control with a simple open-loop strategy, which does not require sensing of the velocity and thermal fields.

In suboptimal control theory, the instantaneous spatial distribution of a control input is determined so as to minimize a prescribed cost function at the next computational time step by taking into account only short-term dynamics, i.e. linear processes. Hence, the obtained control input is not necessarily optimal for a long time horizon. Indeed, the travelling-wave-like control input and the resultant control performance reported in Hasegawa & Kasagi (2011) significantly depend on the size of the computational domain. In the present study, the control input is optimized by taking into account turbulent dynamics within a finite time horizon based on optimal control theory (Abergel & Temam 1990; Bewley, Moin & Temam 2001). Such a control input generally results in much better control performance than the suboptimal control input assuming a vanishingly small time horizon. Specifically, simultaneous achievement of heat transfer augmentation and drag reduction is first demonstrated in the present study. In addition, the present control input is characterized by a travelling-wave-like control input in analogy to that obtained in Hasegawa & Kasagi (2011), but almost independent of the dimension of the computational domain. This allows us to discuss the scaling of the optimal travelling-wave mode for dissimilar heat transfer enhancement.

We will proceed as follows: in § 2, the numerical conditions and the optimization procedures are described. The control results are shown in § 3, and then the detailed mechanisms of dissimilarity are discussed in § 4. The scaling of the optimal travelling wave for dissimilar control is addressed in § 5. Finally, the present study is summarized in § 6.

2. Calculation conditions and mathematical formulation

2.1. *Governing equations and boundary conditions*

In order to derive a general control strategy, we consider one of the most canonical flow systems, namely a fully developed turbulent channel flow as shown in figure 1. The streamwise, wall-normal and spanwise directions are denoted by x_1, x_2 and x_3, respectively. A periodic boundary condition is employed for the x_1 and x_3 directions. The origin of x_2 is located at the centre of the channel, so that the location of the bottom and top walls correspond to $x_2 = -1$ and 1, respectively. The total volume of the computational domain is V_Ω, whereas the domain boundary is expressed by Γ, the subscript of which represents the normal direction.

Typically, the temperature difference between the wall and the fluid is around 5–10 K in a heat exchanger. This indicates that the bulk Richardson number Ri_b is of order 10^{-3} for typical working fluids such as air and water. According to previous direct numerical simulations (DNS) (e.g. Iida & Kasagi 1997; Iida, Kasagi & Nagano 2002), the buoyancy starts to affect the friction coefficient and the Nusselt number when $Ri_b > 10^{-1}$. Hence, in the present study, the temperature is treated as a passive scalar so that no buoyancy effects arise. In addition, the fluid properties are assumed constant. In this case, the velocity and scalar fields are governed by the following

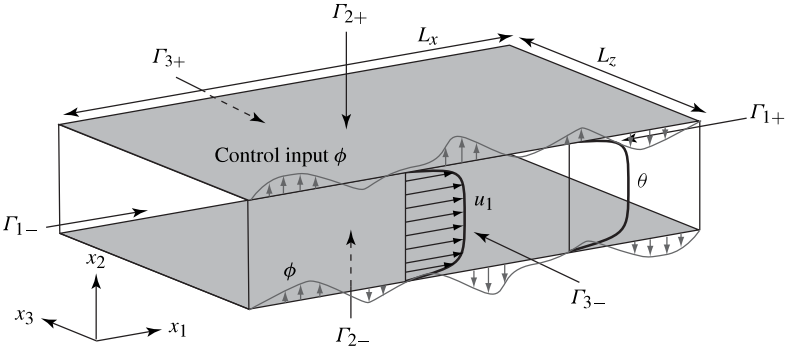

FIGURE 1. Computational domain, its boundaries and coordinate system.

Navier–Stokes, continuity and energy transport equations:

$$\frac{\partial u_i}{\partial t} + \frac{\partial u_j u_i}{\partial x_j} = -\frac{\partial p}{\partial x_i} + \frac{1}{Re}\frac{\partial^2 u_i}{\partial {x_j}^2}, \tag{2.1}$$

$$\frac{\partial u_i}{\partial x_i} = 0, \tag{2.2}$$

$$\frac{\partial \theta}{\partial t} + \frac{\partial u_j \theta}{\partial x_j} = \frac{1}{PrRe}\frac{\partial^2 \theta}{\partial x_j^2} + Q, \tag{2.3}$$

where u_i, p and θ are the ith velocity component, the static pressure and the temperature, respectively. Throughout this paper, all quantities are normalized by the bulk mean velocity U_b^*, the channel half-width δ^*, and the temperature difference between the bulk fluid and the wall, $\Theta_b^* - \Theta_w^*$, while a quantity with an asterisk represents a dimensional quantity. The Reynolds number is defined as $Re = U_b^* \delta^* / \nu^*$, where ν^* is the kinematic viscosity of fluid. The Prandtl number is the ratio of ν^* and the thermal diffusivity α^*, i.e. $Pr = \nu^*/\alpha^*$. The last term on the right-hand side of (2.3) represents heat source Q, which is generally a function of space and time.

Although various thermal boundary conditions exist in real applications, we consider an ideal case where the averaged transport equations for streamwise momentum and heat become identical. Namely, we assume uniform heat generation in the fluid, i.e. $Q = \text{const}$, and it is set to be identical to the mean pressure gradient driving the flow:

$$Q(x_1, x_2, x_3, t) = -\frac{\partial \overline{p}}{\partial x_1}, \tag{2.4}$$

where the overbar represents averaging over the homogeneous directions, i.e. x_1 and x_3, and also time t. In addition, Pr is set to be unity throughout this paper. Consequently, the averaged momentum and heat transport equations have identical forms:

$$-\frac{\partial \overline{p}}{\partial x_1} = \frac{\partial}{\partial x_2}\left(\overline{u_1' u_2'} - \frac{1}{Re}\frac{\partial \overline{u_1}}{\partial x_2}\right), \tag{2.5}$$

$$Q = -\frac{\partial \overline{p}}{\partial x_1} = \frac{\partial}{\partial x_2}\left(\overline{\theta' u_2'} - \frac{1}{Re}\frac{\partial \overline{\theta}}{\partial x_2}\right). \tag{2.6}$$

We consider local wall blowing/suction with zero net mass flux as a control input. For the tangential velocity components and the temperature, we impose the no-slip

and constant-temperature conditions at the two walls. The resultant wall boundary conditions are described as

$$u_i|_{\Gamma_{2\pm}} = \phi n_i, \tag{2.7}$$

$$\theta|_{\Gamma_{2\pm}} = 0. \tag{2.8}$$

Here, the control input, i.e. the wall-normal velocity component imposed at the wall, is denoted by ϕ, the sign of which is defined to be positive when the applied control input is directed towards the outer normal vector n_i at the boundaries of the fluid domain. Throughout this paper, ϕ is normalized by the bulk mean velocity.

It should be noted that the wall boundary conditions of the streamwise velocity component and the temperature remain similar even in the controlled flow, i.e. $u_1 = \theta = 0$ at the two walls. As is evident from (2.5) and (2.6), in order to have dissimilar solutions of $\overline{u_1}$ and $\overline{\theta}$, dissimilarity between $\overline{u_1' u_2'}$ and $\overline{\theta' u_2'}$ is mandatory. Such an ideal flow condition is suitable for investigating the dissimilarity caused by the continuity constraint on the velocity field, since the other possible sources of dissimilarity are all removed (Kasagi *et al.* 2012). It can also be considered as the most difficult situation in which to achieve dissimilar heat transfer enhancement due to the strong similarity in the governing equations and boundary conditions for momentum and heat.

The uniform heat generation considered in the present study is typified by Joule heating of an electrolysis solution. Moreover, in order to mimic the velocity and thermal conditions inside a heat exchanger, a constant-heat-flux condition is often considered. In this case, the resultant dimensionless energy transport equation has an apparent heat source term (see e.g. Kasagi, Kuroda & Tomita 1992), which is proportional to the streamwise velocity component. Although it is not exactly equivalent to the present thermal condition, the thermal field is found to be rather insensitive to the profile of the heat source across the channel due to strong mixing of turbulence as discussed in Kasagi *et al.* (2012). Hence, the present uniform heating can be considered as the first-order approximation of a heat and fluid flow condition inside a heat exchanger. In addition, the thermal conductivity of gas is generally much smaller than those of liquid and solid, so that the overall heat transfer performance is mostly limited by the gas-phase heat transfer in real applications. Given that the Prandtl number of air is close to unity under the standard condition, the present thermal condition is considered to be not only beneficial for fundamental investigation, but also closely linked to practical problems.

Once the flow and thermal fields reach fully developed states, the wall friction balances with the mean pressure gradient. Similarly, the wall heat flux matches the heat source. Since the heat source is set to be identical to the mean pressure gradient in the present condition (see (2.4)), the wall heat flux always follows the wall friction. Meanwhile, the energy transport equation (2.3) and the thermal boundary conditions (2.8) at the two walls are all linear in terms of θ. This means that any dimensionless temperature statistics including the Stanton number defined below are independent of the magnitude of the heat source, and thereby are not directly influenced by the magnitude of the wall friction, but only through modification of turbulent transport mechanisms. Indeed, in the present optimal control, it is demonstrated that the Stanton number is significantly increased while the wall friction is kept smaller than the uncontrolled value.

2.2. *Control performance indices*

Following Hasegawa & Kasagi (2011), the bulk veclocity U_b^* and the bulk temperature Θ_b^* are respectively defined as the following cross-sectional averages of flow rate and temperature:

$$U_b^* = \frac{1}{V_\Omega^*} \int_\Omega u_1^* \, \mathrm{d}V, \tag{2.9}$$

$$\Theta_b^* = \frac{1}{V_\Omega^*} \int_\Omega \theta^* \, \mathrm{d}V. \tag{2.10}$$

As the indices of heat transfer and pressure loss, the following Stanton number St and friction coefficient C_f are defined:

$$St = \frac{q_w^*}{\rho^* C_p^* U_b^* \left(\Theta_b^* - \Theta_w^*\right)}, \tag{2.11}$$

$$C_f = \frac{\tau_w^*}{\frac{1}{2}\rho^* U_b^{*2}}, \tag{2.12}$$

where q_w^* and τ_w^* are wall heat flux and skin friction, respectively. The fluid density is denoted by ρ^*, while C_p^* is the thermal capacity of the fluid.

If the profiles of the averaged streamwise velocity and temperature are similar, $2St$ is exactly equal to C_f at $Pr = 1$. Therefore, we define an analogy factor as

$$A = \frac{2St}{C_f}. \tag{2.13}$$

Physically, A represents heat transfer per unit pumping power. The main objective in dissimilar control is to increase A from unity by manipulating turbulence.

In active control, additional power consumption is required for the control itself. In the present study, however, the intensity of the control input is commonly kept small ($\phi_{rms} \leqslant 0.05$), so that the ideal power consumption of actuators does not significantly affect the overall control performance. Hence, we employ A defined in (2.13) as a primary control performance index. The ideal power consumption of actuators and the heat transfer enhancement per unit total power consumption in the present control are summarized in appendix A.

2.3. *Application of optimal control theory to dissimilar heat transfer enhancement*

In the present study, optimal control theory, which was successfully applied to friction drag reduction control by Bewley *et al.* (2001), is extended to dissimilar heat and momentum transfer control. In this framework, a cost functional is first defined, and then a control input is iteratively updated so as to minimize the cost function within a prescribed time horizon. The correction of a control input in each iteration is obtained by solving the adjoint velocity and thermal fields backward in time. Ideally, the time horizon should be long enough to cover the whole lifetime of turbulence dynamics, but it is not computationally trackable. Therefore, it is common to choose an intermediate finite time horizon T as shown in figure 2. Once a control input converges, the time horizon is advanced by T_a, and then a new optimization procedure in the next time horizon starts. In the following, we define the cost functional, derive the adjoint equations, and describe the optimization procedures without getting into the mathematical details, which can be found in other literature such as Abergel & Temam (1990) and Bewley *et al.* (2001).

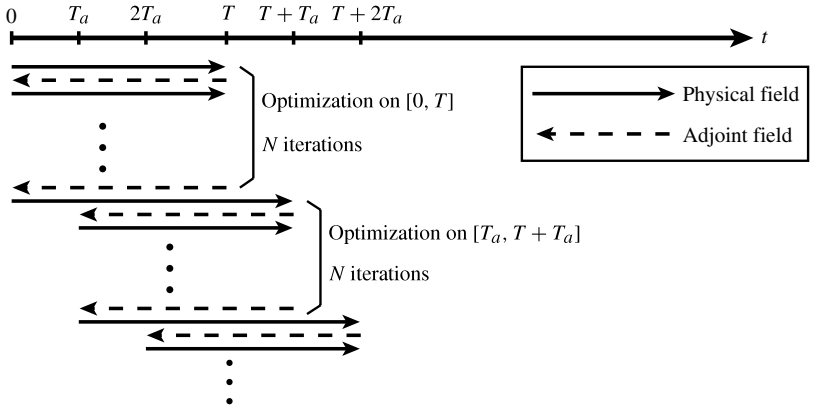

FIGURE 2. Schematic of optimization procedure. In each time horizon, the evolution of velocity and thermal fields is solved for a preliminary control input as shown by the solid arrows, which is followed by adjoint computation depicted by the reversed dashed arrows. The adjoint field is solved backward in time, since its initial condition is given at the end of the time horizon. Based on the results of the adjoint field, the control input is iteratively updated. Once the control input converges, the time horizon is advanced by T_a and then a new optimization procedure starts.

2.3.1. *Defining the cost functional*

We define a cost functional as follows:

$$J = \kappa \int_0^T \int_{\Gamma_{2\pm}} \frac{1}{2}\phi^2 \,\mathrm{d}S\,\mathrm{d}t - A$$
$$\approx \kappa \int_0^T \int_{\Gamma_{2\pm}} \frac{1}{2}\phi^2 \,\mathrm{d}S\,\mathrm{d}t - \frac{\displaystyle\int_0^T \int_{\Gamma_{2\pm}} -\frac{\partial\theta}{\partial n}\,\mathrm{d}S\,\mathrm{d}t}{\displaystyle\int_0^T \int_{\Gamma_{2\pm}} -\frac{\partial u}{\partial n}\,\mathrm{d}S\,\mathrm{d}t}, \tag{2.14}$$

where $t = 0$ corresponds to the beginning of the time horizon and $\mathrm{d}S$ is infinitesimal area of the boundary. The first term represents the cost of control, while the second term is exactly the quantity we attempt to enhance, i.e. the analogy factor. Hence, under this cost functional, the control input is optimized so as to maximize A with the smallest intensity of wall blowing/suction. Ideally, A has to be determined by the ratio of $2St$ and C_f integrated over a sufficiently long period. Since optimal control theory takes into account only flow dynamics within a finite time horizon, however, A is approximated by the integrals within the time horizon as shown in the second line of (2.14). The weight coefficient κ corresponds to the relative cost of the control input. In the present study, the intensity of the control input is changed by setting different values of κ. The actual values of T and κ employed in the present study are summarized in § 2.4.

In addition to (2.14), different forms of cost functional are also considered. It is found that the present cost functional results in the best control performance (see appendix B). Hence, the present paper focuses on the results obtained under the cost functional (2.14).

2.3.2. *Derivation of adjoint equations and gradient of cost functional*

For ease of notation, the flow state $\boldsymbol{\psi}$, the flow perturbation state $\boldsymbol{\psi}'$ and the adjoint state $\boldsymbol{\psi}^*$ are expressed as the following vector forms:

$$\boldsymbol{\psi} = \begin{pmatrix} p \\ u_i \\ \theta \end{pmatrix}, \quad \boldsymbol{\psi}' = \begin{pmatrix} p' \\ u_i' \\ \theta' \end{pmatrix}, \quad \boldsymbol{\psi}^* = \begin{pmatrix} p^* \\ u_i^* \\ \theta^* \end{pmatrix}. \tag{2.15}$$

The governing equations (2.1)–(2.3) for the velocity and thermal fields can be written in a functional form as

$$N(\boldsymbol{\psi}) = \begin{pmatrix} \dfrac{\partial u_i}{\partial x_i} \\ \dfrac{\partial u_i}{\partial t} + \dfrac{\partial u_j u_i}{\partial x_j} - \dfrac{1}{Re}\dfrac{\partial^2 u_i}{\partial {x_j}^2} + \dfrac{\partial p}{\partial x_i} \\ \dfrac{\partial \theta}{\partial t} + \dfrac{\partial u_j \theta}{\partial x_j} - \dfrac{1}{RePr}\dfrac{\partial^2 \theta}{\partial x_j^2} - Q \end{pmatrix} = \mathbf{0}. \tag{2.16}$$

Then, we consider the perturbation field $\boldsymbol{\psi}'$ of the velocity and thermal fields induced by a small change of a control input ϕ. Following Bewley *et al.* (2001), the perturbation is defined by the Frechét differential of the original flow state $\boldsymbol{\psi}$ as

$$\boldsymbol{\psi}' \triangleq \lim_{\epsilon \to 0} \frac{\boldsymbol{\psi}(\phi + \phi'\epsilon) - \boldsymbol{\psi}(\phi)}{\epsilon}, \tag{2.17}$$

where ϵ is an infinitesimal constant.

Since both the original and perturbed flow states satisfy (2.16), the following linear equation for $\boldsymbol{\psi}'$ is obtained:

$$N'(\boldsymbol{\psi}') = \begin{pmatrix} \dfrac{\partial u_i'}{\partial x_i} \\ \dfrac{\partial u_i'}{\partial t} + \dfrac{\partial}{\partial x_j}\left(u_j u_i' + u_j' u_i\right) - \dfrac{1}{Re}\dfrac{\partial^2 u_i'}{\partial {x_j}^2} + \dfrac{\partial p'}{\partial x_i} \\ \dfrac{\partial \theta'}{\partial t} + \dfrac{\partial}{\partial x_j}\left(u_j \theta' + u_j' \theta\right) - \dfrac{1}{RePr}\dfrac{\partial^2 \theta'}{\partial x_j^2} \end{pmatrix} = \mathbf{0}, \tag{2.18}$$

where the wall boundary conditions are given by

$$u_i' = -\phi' n_i, \quad \theta' = 0 \quad \text{on } \Gamma_{\pm 2}, \tag{2.19}$$

$$u_i' = \mathbf{0}, \quad \theta' = 0 \quad \text{at } t = 0. \tag{2.20}$$

In (2.18), the products between perturbations are all neglected since the perturbation is assumed to be sufficiently small. Although (2.18)–(2.20) indicate a linear relationship between ϕ' and $\boldsymbol{\psi}'$, it is not straightforward to derive the explicit relationship between ϕ' and the resultant change of the cost functional J'. In order to overcome this difficulty, the adjoint velocity and thermal fields are introduced.

The flow optimization can generally be viewed as a minimization problem of a cost functional J under the constraints on the flow states, i.e. the governing equations and the boundary conditions of the flow and thermal fields. This is equivalent to

minimizing the following Hamiltonian H:

$$H = J - \langle N(\boldsymbol{\psi}), \boldsymbol{\psi}^* \rangle, \tag{2.21}$$

where the adjoint state $\boldsymbol{\psi}^*$ corresponds to the Lagrangian multiplier.

The Frechét differential of (2.21) leads to

$$\begin{aligned} \frac{\mathscr{D}H}{\mathscr{D}\phi}\phi' &= J' - \langle N'(\boldsymbol{\psi}'), \boldsymbol{\psi}^* \rangle \\ &= J' - \langle \boldsymbol{\psi}', N^*(\boldsymbol{\psi}^*) \rangle - b, \end{aligned} \tag{2.22}$$

where N^* is the adjoint operator of N'. We impose the following relationship for the adjoint field:

$$N^*(\boldsymbol{\psi}^*) = \begin{pmatrix} -\dfrac{\partial u_i^*}{\partial x_i} \\ -\dfrac{\partial u_i^*}{\partial t} - u_j\left(\dfrac{\partial u_i^*}{\partial x_j} + \dfrac{\partial u_j^*}{\partial x_i}\right) - \dfrac{1}{Re}\dfrac{\partial^2 u_i^*}{\partial x_j{}^2} - \dfrac{\partial p^*}{\partial x_i} - \theta\dfrac{\partial \theta^*}{\partial x_i} \\ -\dfrac{\partial \theta^*}{\partial t} - u_j\dfrac{\partial \theta^*}{\partial x_j} - \dfrac{1}{RePr}\dfrac{\partial^2 \theta^*}{\partial x_j^2} \end{pmatrix} = \mathbf{0}, \tag{2.23}$$

so that the second term on the right-hand side of (2.22) vanishes. The first term on the right-hand side of (2.22) is the Frechét differential of the cost functional, and can be written as

$$\begin{aligned} J' = \kappa \int_0^T \int_{\Gamma_{2\pm}} \phi\phi' \,\mathrm{d}S\,\mathrm{d}t \\ + \frac{A}{TS_{\Gamma_{2\pm}}\tau_w}\int_0^T \int_{\Gamma_{2\pm}} -\frac{\partial u'}{\partial n}\,\mathrm{d}S\,\mathrm{d}t - \frac{A}{TS_{\Gamma_{2\pm}}q_w}\int_0^T \int_{\Gamma_{2\pm}} -\frac{\partial \theta'}{\partial n}\,\mathrm{d}S\,\mathrm{d}t, \end{aligned} \tag{2.24}$$

where $S_{\Gamma 2\pm}$ represents the boundary area of $\Gamma_{2\pm}$. The third term on the right-hand side of (2.22) is called a boundary term, since it includes only boundary integrals as shown below:

$$\begin{aligned} b = \int_\Omega (u_j' u_j^* + \theta'\theta^*)\Big|_{t^+=0}^{t^+=T} \mathrm{d}V \\ + \int_0^T \int_{\Gamma_{2\pm}} n_j \left[p^* u_j' + u_j^* p' + u_i^*(u_j u_i' + u_i u_j') - \frac{1}{Re}\left(u_i^*\frac{\partial u_i'}{\partial x_j} - u_i'\frac{\partial u_i^*}{\partial x_j}\right) \right. \\ \left. + (u_j'\theta + u_j\theta')\theta^* - \frac{1}{RePr}\left(\theta^*\frac{\partial \theta'}{\partial x_j} - \theta'\frac{\partial \theta^*}{\partial x_j}\right)\right] \mathrm{d}S\,\mathrm{d}t. \end{aligned} \tag{2.25}$$

The terminal and boundary conditions for the adjoint state are given by

$$\boldsymbol{\psi}^*|_{t=T} = \mathbf{0}, \tag{2.26}$$

$$u_i^*|_{\Gamma_{2\pm}} = A\frac{Re}{TS_{\Gamma_{2\pm}}\tau_w}\delta_{1i}, \tag{2.27}$$

$$\theta^*|_{\Gamma_{2\pm}} = -A\frac{RePr}{TS_{\Gamma_{2\pm}}q_w}, \tag{2.28}$$

so that the integrand of (2.22) is eventually factorized by ϕ' as follows:

$$\begin{aligned}\frac{\mathscr{D}H}{\mathscr{D}\phi}\phi' &= J' - \langle \boldsymbol{\psi}', N^*(\boldsymbol{\psi}^*)\rangle - b \\ &= \kappa \int_0^T \int_{\Gamma_{2\pm}} \phi\phi' \,\mathrm{d}S\,\mathrm{d}t - \frac{A}{\tau_w}\int_0^T \int_{\Gamma_{2\pm}} \frac{\partial u'}{\partial n}\,\mathrm{d}S\,\mathrm{d}t + \frac{A}{q_w}\int_0^T \int_{\Gamma_{2\pm}} \frac{\partial \theta'}{\partial n}\,\mathrm{d}S\,\mathrm{d}t \\ &\quad - \int_0^T \int_{\Gamma_{2\pm}} \left[p^*\phi' - \frac{A}{\tau_w}\frac{\partial u_i'}{\partial n} + \frac{A}{q_w}\frac{\partial \theta'}{\partial n}\right] \mathrm{d}S\,\mathrm{d}t \\ &= \int_0^T \int_{\Gamma_{2\pm}} (\kappa\phi - p^*)\,\phi' \,\mathrm{d}S\,\mathrm{d}t. \end{aligned} \tag{2.29}$$

The final form of (2.29) guarantees that correcting the control input by $\phi' = -(\kappa\phi - p^*)$ decreases H. Therefore, after solving the adjoint field, the control input is updated as follows:

$$\phi^{n+1} = \phi^n - \beta(\kappa\phi^n - p^*), \tag{2.30}$$

where the superscript represents the number of iteration, while β is a relaxation coefficient. In the present study, β is determined so that $|\phi^{n+1} - \phi^n| < 3.0 \times 10^{-3}$. This increases β as the control input converges. Hence, $\beta < 8$ is also imposed throughout the optimization procedure. In general, the simple gradient algorithm given by (2.30) does not converge efficiently, so that a more sophisticated scheme such as a conjugate gradient method is often employed. In the present study, however, the optimal control input is dominated by a single sinusoidal wave travelling at a constant phase velocity, so that (2.30) with around 10 iterations is sufficient to obtained a converged control input. It is confirmed that further increase of iteration number does not significantly change the control performance or the main features of the resultant travelling-wave-like control input.

2.4. *Numerical scheme and conditions*

The governing equations (2.1)–(2.3) for the velocity and thermal fields are solved by DNS with a second-order finite-volume method. For the temporal discretization, the Crank–Nicolson method is used for the diffusion terms, while the third-order low-storage Runge–Kutta method (Spalart, Moser & Rogers 1991) is used for nonlinear terms. A fractional step method (Rai & Moin 1991) is used for decoupling the velocity and pressure fields. The present DNS code is based on the code originally developed by Satake & Kasagi (1996). It was validated through thorough comparisons with existing databases and successfully applied to skin-friction-drag-reduction control (Frohnapfel, Hasegawa & Kasagi 2010). All calculations are conducted under a constant bulk mean velocity and the Reynolds number is usually set to be $Re = 2284$, which corresponds to the friction Reynolds number of $Re_\tau = u_\tau^*\delta^*/\nu^* = 150$ in the uncontrolled flow. In order to investigate the Reynolds number effects, we also consider two different lower and higher Reynolds numbers, i.e. $Re = 1452$ and 4980, which are equivalent to $Re_\tau = 100$ and 300 in the uncontrolled flow, respectively. Due to the similarity in the mathematical form of (2.16) and (2.23), essentially the same numerical method is used for solving the adjoint field. Note that the adjoint equation is solved backward in time from $t = T$ to $t = 0$, as the terminal condition is given for the adjoint field (see (2.26)).

Table 1 summarizes the present numerical conditions. In uncontrolled flow, it is known that C_f obtained from existing databases can be well predicted by the so-called

https://doi.org/10.1017/jfm.2013.436 Published online by Cambridge University Press

Re	L_x	L_z	(N_x, N_y, N_z)	$(\Delta x, \Delta y, \Delta z)$	$\kappa \times 10^2$	ϕ_{rms}	$C_f \times 10^3$	$St \times 10^3$	A	Case
2284	2.5π	π	(64, 129, 64)	(18.4, 0.18–5.7, 7.4)	—	0.0	9.01	4.60	1.02	Uncontrolled
2284	2.5π	π	(64, 129, 64)	(18.4, 0.18–5.7, 7.4)	0.4	0.05	6.90	9.38	2.72	Case 1
2284	2.5π	π	(128, 129, 128)	(9.2, 0.18–5.7, 3.7)	0.4	0.04	6.84	8.04	2.35	Case 1F
2284	5π	2π	(128, 129, 128)	(18.4, 0.18–5.7, 7.4)	1.6	0.04	7.01	8.03	2.29	Case 1W
2284	2.5π	π	(64, 129, 64)	(18.4, 0.18–5.7, 7.4)	2.0	0.03	6.87	7.28	2.12	Case 2
2284	2.5π	π	(64, 129, 64)	(18.4, 0.18–5.7, 7.4)	4.0	0.02	6.99	5.87	1.68	Case 3
1452	2.5π	π	(64, 129, 64)	(12.3, 0.12–3.8, 4.9)	—	0.0	9.30	4.70	1.01	Uncontrolled
1452	2.5π	π	(64, 129, 64)	(12.3, 0.12–3.8, 4.9)	0.3	0.17	7.42	7.15	3.86	Case 4
4980	2.5π	π	(128, 129, 128)	(18.4, 0.36–11, 7.4)	—	0.0	7.67	4.05	1.06	Uncontrolled
4980	2.5π	π	(128, 129, 128)	(18.4, 0.36–11, 7.4)	0.4	0.03	6.90	6.23	1.81	Case 5

TABLE 1. Computational domain size, number of grid points, grid spacings, κ and the resultant ϕ_{rms} for all cases considered.

Dean's formula given by $C_f = \alpha Re^{-1/4}$, where the promotional coefficient α is 0.59 for low Reynolds numbers (see e.g. Kim, Moin & Moser 1987). At $Re = 2284$, the computation with the relatively coarse grid of case 1 overestimates C_f by around 6 %, whereas it converges to the value predicted by the Dean's formula within an error of 2 % in case 1F. Since the optimization of the control input requires a number of iterations of each time horizon and huge memory capacity to store the complete dataset of the velocity and thermal fields, the optimal control of turbulent flows generally requires huge computational resource. Hence, our strategy is to extract general features of the optimal control input for dissimilar heat transfer enhancement through computations with a relatively small domain and coarse grid system. As will be shown later, the effects of the grid spacing and the computational domain are found to be minor. This could be explained by the fact that the optimal control input is commonly characterized by a travelling wave which has relatively large wavelength, and therefore the dissimilarity is mainly caused by large-scale velocity and thermal fluctuations, which can be resolved by the present grid spacing. In § 5, the effects of the wavelength of a travelling-wave-like control input on the control performance are examined in detail with a finer grid system.

The intensity of the control input is systematically decreased by increasing κ from 0.004 to 0.04 in cases 1–3, so that the r.m.s. value of the control input changes from 2 % to 5 % of the bulk mean velocity (see table 1). For $\kappa = 0.004$, computations with doubled grid points and doubled domain size (Cases 1F and 1W) are also conducted to verify the present numerical condition.

Instantaneous snapshots of the velocity and thermal fields are stored every $t^+ = 5$ in the computation of the physical field. In the adjoint computation, the velocity and thermal fields at a certain time step are obtained by linear interpolation of two neighbouring snapshots. It is also possible to further increase the time interval between two neighbouring snapshots if one can afford to conduct an additional DNS by using the nearest snapshot as an initial condition in each adjoint computation.

Although there is tendency that larger T results in better control performance up to $T^+ \approx 100$ of the uncontrolled flow, it is found that further increase of the time horizon often makes the adjoint computation diverge. This could be attributed to the fact that the mathematical derivation of the optimal control input is based on the linearized perturbation equation (2.18), where the perturbation of a flow state induced by a small change of a control input is assumed to remain sufficiently small during the time horizon, so that all nonlinear terms can be neglected. However, it is well known that a small disturbance grows very rapidly in turbulent flow due to its nonlinear nature. This implies that (2.18) is invalid for a large time horizon. Hence, in the present study, the time horizon is set to be $T^+ = 100$. Note that this period is comparable with that employed in Bewley *et al.* (2001), where the control input is successfully optimized for skin-friction drag reduction at a low Reynolds number. Once the control input is converged within a time horizon, the time horizon is advanced by $T_a^+ = T^+/10 = 10$ (see figure 2).

3. Control results

3.1. *Control performance*

In this section, we present the control results and also fundamental velocity and temperature statistics of the controlled flows. For simplicity of description, x, y and z are used instead of x_1, x_2 and x_3 as the three coordinates hereafter. Accordingly, the corresponding velocity components are denoted by u, v and w, respectively. First, the

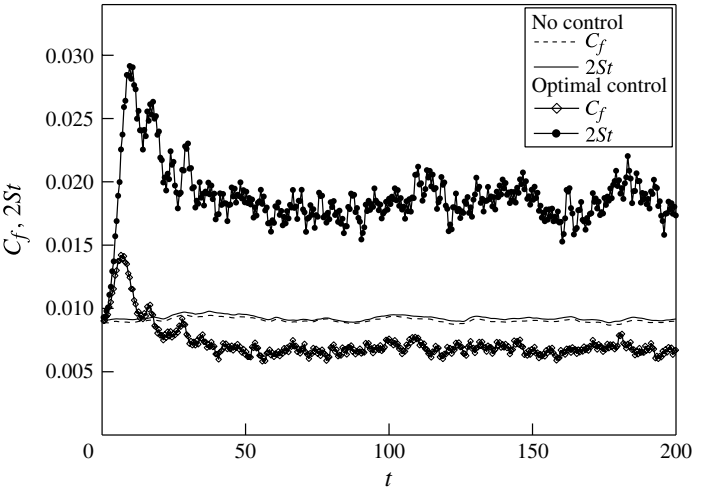

FIGURE 3. Time traces of C_f and St with optimal control, for case 1.

time traces of C_f and $2St$ after the onset of control at $t = 0$ in case 1 are shown in figure 3. The data of the uncontrolled flow are also plotted for comparison. It is confirmed that the Reynolds analogy, i.e. $2St = C_f$, holds quite well in the uncontrolled flow. When the optimal control is applied, St is more than doubled after the transient period of $t \sim 50$, while C_f is suppressed. Hence, significant dissimilarity is observed. All the statistics shown hereafter are obtained by integrating from $t = 102$ to 203 so as to remove the effects of the initial transient.

In figure 4, the time-averaged C_f, St and the resultant A are plotted as a function of the r.m.s. value of the control input for cases 1, 1F and 1W. The results of the suboptimal control (Hasegawa & Kasagi 2011) are also plotted for comparison. Note that C_f and St are both normalized by C_{f0} and St_0, where the subscript of 0 represents an uncontrolled value. The values of C_f and St in all cases are also listed in table 1. It is found that C_f is commonly decreased from the uncontrolled value by 24 % when $\phi_{rms} > 0.02$. In contrast, St is monotonically enhanced with increasing ϕ_{rms}. More specifically, St is more than doubled at $\phi_{rms} \approx 0.05$. Consequently, the analogy factor is increased to as high as $A = 2.7$.

As shown in figure 4, the analogy factor achieved in the present optimal control is larger than that obtained in the suboptimal control (Hasegawa & Kasagi 2011), although A increases almost in proportion to ϕ_{rms} in both controls. This is because C_f in the suboptimal control is significantly larger than that in the optimal control. In the suboptimal control, C_f is enhanced, whereas drag reduction is achieved in the optimal control. It should be noted that the drag reduction rate obtained in the present optimal control is comparable to that achieved in a typical drag reduction scheme such as opposition control (Choi, Moin & Kim 1994). However, Hasegawa & Kasagi (2011) showed that applying opposition control does not cause dissimilarity: the heat transfer is also decreased at almost the same rate. Indeed, the present control input is entirely different from that in opposition control. To the authors' knowledge, the simultaneous achievement of heat transfer enhancement and drag reduction is demonstrated for the first time.

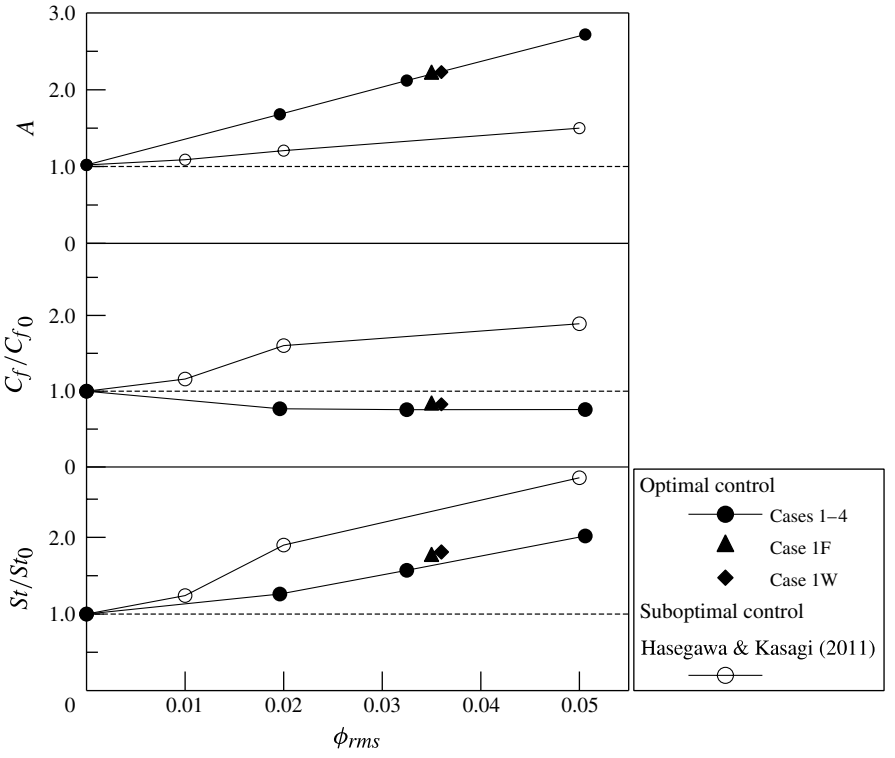

FIGURE 4. C_f/C_{f0}, St/St_0 and analogy factor as a function of the r.m.s. value of a control input. The data of $\phi_{rms} = 0$ correspond to the uncontrolled values.

In figure 4, the results obtained with finer grids and larger computational domain in cases 1F and 1W are also shown. In the present study, the intensity of the control input is determined as a result of computation by setting different values of κ in (2.14), so that it is difficult to compare the results at exactly the same value of ϕ_{rms}. However, it is confirmed that the effects of the grid resolution and the domain size on the control results are insignificant.

3.2. *Fundamental statistics*

Hereafter, we present velocity and temperature statistics in case 1 unless otherwise stated, since the general trend is essentially the same in the other cases. In figure 5, the mean velocity and temperature profiles in the uncontrolled and controlled flows are plotted. In the uncontrolled flow, the profiles of $\overline{u}$ and $\overline{\theta}$ are almost identical. This is consistent with the fact that the Reynolds analogy, i.e. $A = 1$, holds well in the uncontrolled flow. Taking a closer look, however, the profile of $\overline{\theta}$ is slightly more uniform than that of $\overline{u}$ around the channel centre, indicating that the mixing of scalar is stronger than that of momentum even in the uncontrolled flow. As reported in Hasegawa & Kasagi (2011), this small deviation still remains even for sufficiently large integration time. In incompressible fluid, the streamwise velocity fluctuation is redistributed to those of the other components via pressure strain effects, while such a mechanism is absent for a scalar quantity. Indeed, we confirmed that the eddy diffusivity for temperature is slightly larger than the eddy viscosity away from the wall

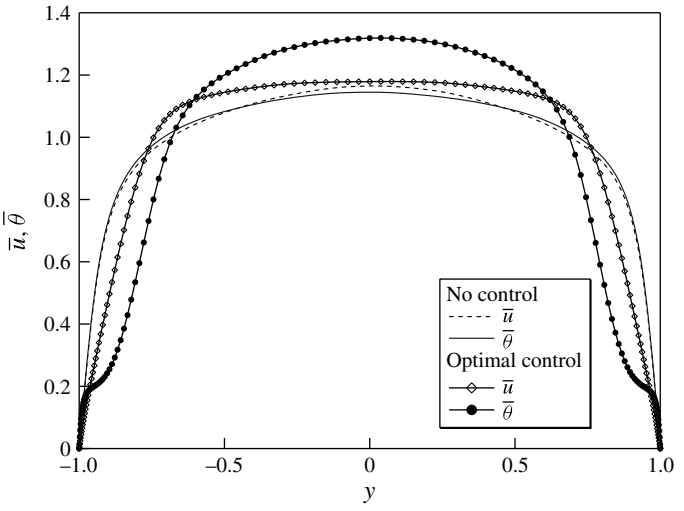

FIGURE 5. Profiles of $\overline{u}$ and $\overline{\theta}$ without control and with optimal control (case 1).

even in the uncontrolled flow. Similar dissimilarity is also observed in experimental measurements of a turbulent boundary layer (e.g. Antonia & Krishnamoorthy 1988). However, this causes little change of A from unity in the uncontrolled flow (see table 1), since the turbulence contributions to St and C_f are quite small in the central region of the channel as suggested by (4.5) and (4.6) below.

Once the control is applied, the temperature gradient at the wall becomes steeper than the velocity gradient. This is consistent with the significant increase of A from unity in the controlled flow. With increasing distance from the wall, both the velocity and temperature are initially kept smaller than those of the uncontrolled flow, and then become larger in the central region.

Since both the mean pressure gradient and the heat source are uniform within the computational domain, the shear stress and the heat flux should be distributed linearly in the y direction (see (2.5) and (2.6)). The shear stress is composed of the viscous and Reynolds stresses, i.e. $(1/Re)\partial\overline{u}/\partial y$ and $-\overline{u'v'}$, while the heat flux is composed of the molecular and turbulent heat fluxes, i.e. $(1/Re)\partial\overline{\theta}/\partial y$ and $-\overline{\theta'v'}$. These profiles in the uncontrolled and controlled flows are plotted in figures 6(a) and 6(b), respectively. The almost linear profiles of the total shear stress and heat flux ensure that the velocity and thermal fields reach a fully developed state. We also note that the total stress and heat flux at the wall are identical to $C_f/2$ and St in the present normalization. In the uncontrolled flow, all distributions of momentum and heat fluxes are almost identical, suggesting the strong similarity between them. In the controlled flow, $-\overline{\theta'v'}$ is significantly larger than $-\overline{u'v'}$ throughout the channel. This causes dissimilarity between the mean velocity and temperature profiles as indicated by (2.5) and (2.6).

3.3. *Control input*

The time evolution of the distribution of the control input in case 1 is shown in figure 7(a–c). The time interval of each figure is $\Delta t = 2$ and the left and right columns show the control input on the top and bottom walls, respectively. Note that a positive value of ϕ represents wall blowing at both walls. The optimal control input is found

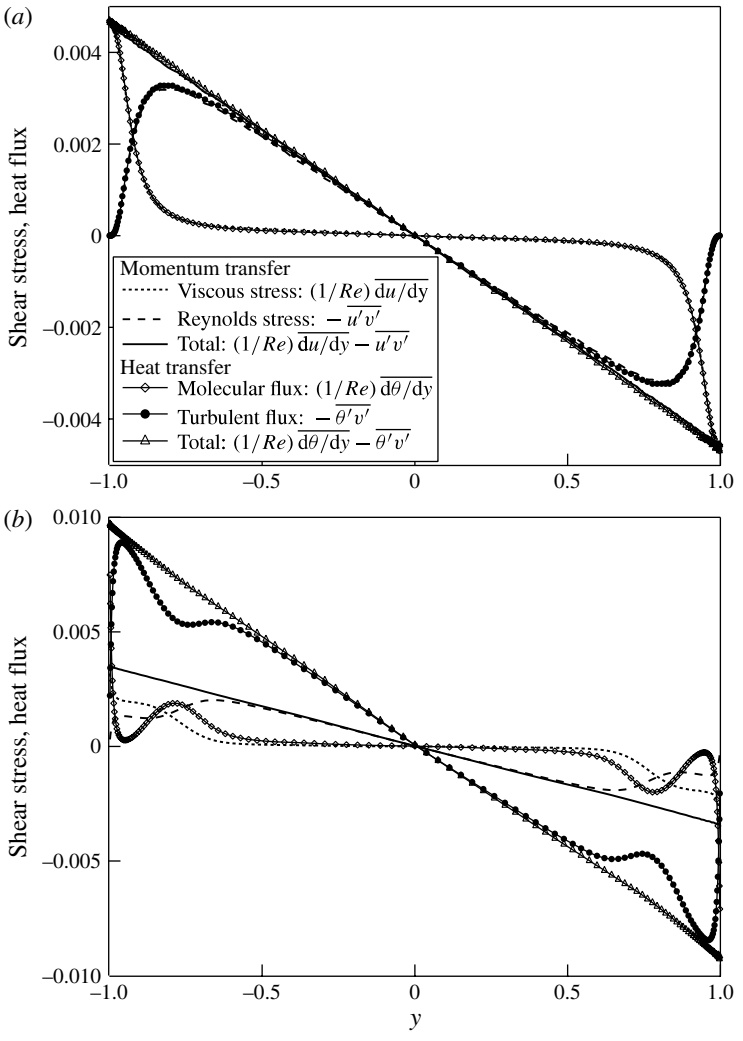

FIGURE 6. Shear stress and heat flux distributions for (*a*) uncontrolled and (*b*) controlled flow in case 1.

to be characterized by a coherent streamwise wave which is almost uniform in the spanwise direction. The wave appears to travel in the downstream direction at almost a constant phase velocity. In addition, the control inputs on both walls are in a varicose mode: wall blowing/suction occurs at the same streamwise location on both walls.

Figures 8(*a*) and 8(*b*) show the spatial spectra of the control input in the streamwise and spanwise directions, respectively. The peaks of the spectra occur at $(k_x, k_z) = (3.2, 0)$, where k_x and k_z are wavenumbers in the streamwise and spanwise directions. It is found that the single sinusoidal mode of $(k_x, k_z) = (3.2, 0)$ contains 66 % of the total energy of the control input. In addition, the phase velocity U_p of the dominant sinusoidal mode of $(k_x, k_z) = (3.2, 0)$ is almost constant and around 30 % of the bulk mean velocity as shown in figure 9.

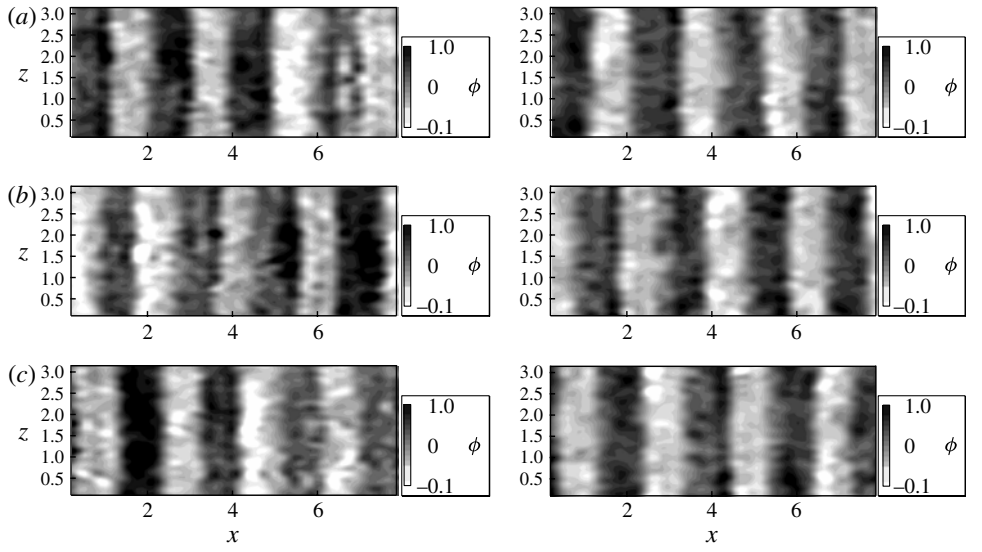

FIGURE 7. Three successive snapshots of instantaneous control input at: (*a*) $t = 198$, (*b*) $t = 200$ and (*c*) $t = 202$. The left and right columns show the distributions on the top and bottom walls, respectively.

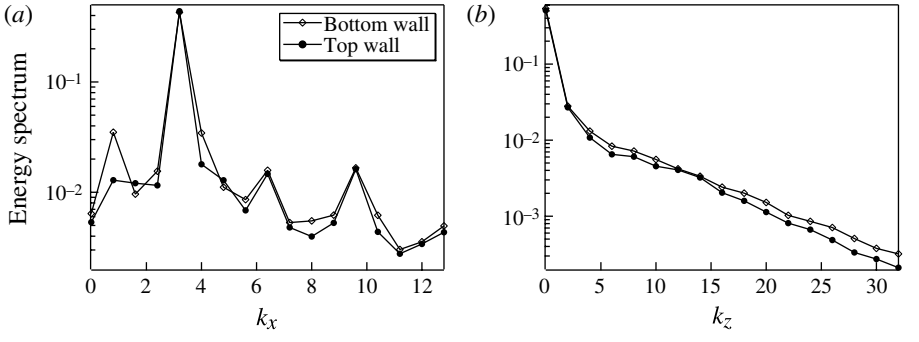

FIGURE 8. Spatial spectra of control input in (*a*) the streamwise and (*b*) spanwise directions in case 1.

4. Mechanisms of dissimilarity

4.1. *Decomposition of coherent and random components*

In optimal control theory, the control input is optimized by taking into account complex turbulence dynamics within a prescribed time horizon, and therefore it generally depends on the instantaneous flow state. In contrast, the optimal control input shown in § 3.3 is characterized by superposition of a dominant coherent travelling wave and weaker random fluctuation. Following the results, we decompose the optimal control input into coherent and random components in order to investigate their quantitative contributions to dissimilar heat transfer enhancement. We define the coherent component of the optimal control input as a component causing dissimilarity regardless of the instantaneous turbulence state. Finding such a coherent mode is key for establishing a open-loop control strategy.

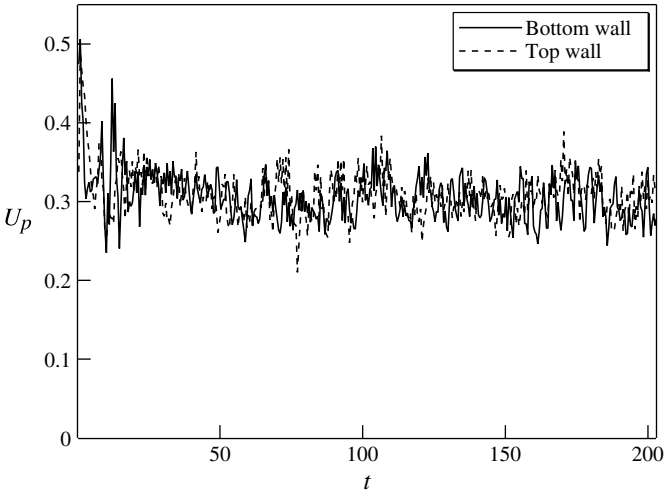

FIGURE 9. Time traces of the phase velocity U_p of the dominant sinusoidal mode $((k_x, k_z) = (3.2, 0))$.

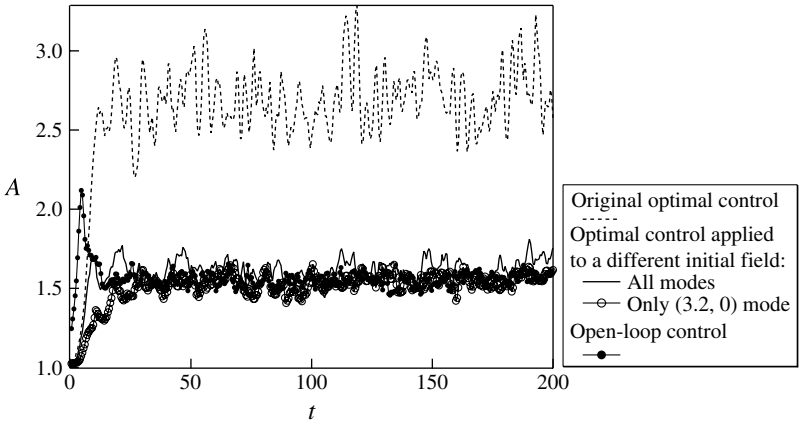

FIGURE 10. Time trace of analogy factor when limited Fourier modes in the optimal control input are applied.

In order to extract the coherent component from the optimal control input, we conduct an ideal computation, where the time series of the control input optimized for a certain initial flow condition is applied to an uncorrelated different initial field. The results are shown in figure 10. As expected, A is reduced from the original value of $A = 2.7$. However, it should be emphasized that the resultant A is still significantly larger than unity, i.e. $A \approx 1.55$. The obtained A is even larger than that achieved by the suboptimal control (Hasegawa & Kasagi 2011) at the same r.m.s. value of the control input. This indicates that the optimal control input contains a coherent component which causes dissimilarity regardless of the instantaneous flow state. Next, we systematically remove Fourier components possessing less energy from the original optimal control input. It is found that A is kept almost unchanged even when all

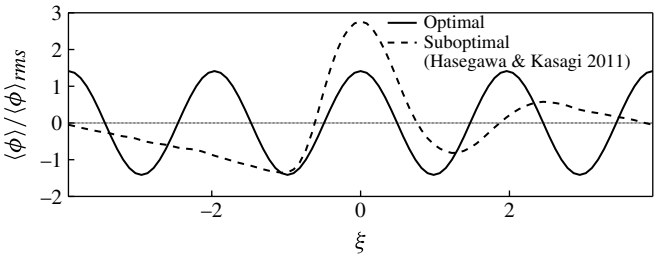

FIGURE 11. Coherent components obtained in the suboptimal and optimal control theories.

	ϕ_{rms}	C_f/C_{f0}	St/St_0	A
Optimal control	0.051	0.757	2.02	2.72
Suboptimal control (Hasegawa & Kasagi 2011)	0.050	2.03	3.05	1.51
Open-loop control based on optimal control	0.043	2.01	3.06	1.55
Open-loop based on suboptimal control	0.043	2.58	3.53	1.38

TABLE 2. Comparison of results obtained by optimal, suboptimal and open-loop controls.

the modes except for the most dominant sinusoidal mode of $(k_x, k_z) = (3.2, 0.0)$ are removed. (see figure 10). The phase velocity and amplitude of the dominant sinusoidal mode are slightly modulated in time around their mean value as shown in figure 9. Hence, we also fix the phase velocity and amplitude of the dominant sinusoidal mode to their mean values. Again, A is not changed. The above series of numerical experiments indicates that the dominant single sinusoidal wave travelling at a constant phase velocity is the coherent component causing dissimilarity. Hereafter, a control applying a single sinusoidal wave of wall blowing and suction with constant amplitude and phase velocity is referred to as an open-loop control.

In Hasegawa & Kasagi (2011), a similar travelling-wave-like control input is obtained through suboptimal control theory. In their case, the coherent input is not a single sinusoidal wave, but is characterized by strong blowing from a narrower spanwise band and weaker suction quite uniformly distributed upstream of the blowing region. They extracted a coherent component by using a conditional averaging technique, and demonstrated that the dissimilarity is achieved by an open-loop control using the extracted coherent input. The coherent components obtained from the suboptimal and optimal control inputs are compared in figure 11, where both the profiles are normalized by their r.m.s. values. Note that the horizontal axis ξ represents the streamwise coordinate and it is appropriately shifted so that $\xi = 0$ corresponds to the location where the wall blowing becomes maximum.

The control performances achieved in the suboptimal, optimal and open-loop controls are summarized in table 2. The friction coefficient and the Stanton number are respectively normalized by C_{f0} and St_0. We note that ϕ_{rms} of the open-loop control is slightly smaller than those in the optimal and suboptimal controls due to the absence of the random component. It is found that the open-loop control based on the present optimal control achieved a higher control performance than that obtained in the

previous suboptimal control at the same r.m.s. value of the control input. Considering that the suboptimal control input is determined based on the complete information of the velocity and thermal fields at every time step, we can conclude that the present open-loop control results in significant dissimilar heat transfer enhancement in spite of its simple control strategy. We also note that the present results in the open-loop control are consistent with the previous ones reported in Min *et al.* (2006), where downstream travelling waves of wall blowing and suction are found to increase C_f. The reduction of C_f in the optimal control implies that the rest of the control input except for a downstream travelling sinusoidal wave plays a critical role in skin-friction drag reduction.

Before closing this subsection, we introduce a phase average with respect to the travelling-wave control input. In Fourier space, the control input can generally be expressed as

$$\phi(x, z, t) = \sum_{k_z} \sum_{k_x} \hat{\phi}(k_x, k_z, t) \exp\{\mathrm{i}(k_x x + k_z z)\}. \tag{4.1}$$

A variable with a hat represents a Fourier coefficient. The phase of the most dominant sinusoidal wave is given by

$$\alpha(t) = \arctan\left[\frac{\mathrm{Im}\{\phi(k_x^d, 0, t)\}}{\mathrm{Re}\{\phi(k_x^d, 0, t)\}}\right], \tag{4.2}$$

where k_x^d is the streamwise wavenumber of the dominant mode. We define the phase averaging with respect to the travelling wave as follows:

$$\langle f \rangle(\xi, y) = \frac{1}{TL_z} \int_0^T \int_0^{L_z} \sum_{n=1}^{N} \frac{1}{N} f\left(\xi + x_d + n\lambda_x^d, y, z, t\right) \mathrm{d}z\, \mathrm{d}t, \tag{4.3}$$

where f is an arbitrary quantity in the computational domain, $x_d(t) = -\alpha(t)/k_x^d$ and $\lambda_x^d (= 2\pi/k_x^d)$, which is the wavelength of the travelling wave. The phase velocity of the dominant wave is given by $U_p = (1/k_x^d)\, \mathrm{d}\alpha/\mathrm{d}t$. Accordingly, the instantaneous value of f can be expressed as $f(x, y, z, t) = \langle f \rangle(\xi, y) + f''(x, y, z, t)$, where f'' is the deviation from the phase average and referred to as a random component throughout this paper. The phase average is further decomposed into the spatial mean and the coherent fluctuation travelling at the same phase velocity: $\langle f \rangle(\xi, y) = \overline{f}(y) + \tilde{f}(\xi, y)$. Consequently, the instantaneous flow quantity can generally be written as a sum of the spatial mean, and the coherent and random fluctuations as follows

$$f(x, y, z, t) = \overline{f}(y) + \tilde{f}(\xi, y) + f''(x, y, z, t). \tag{4.4}$$

4.2. *Contributions of coherent and random components*

Applying triple integration to the averaged momentum and energy transport equations (2.5) and (2.6), the following mathematical relationships for C_f and $2St$ can be derived (Fukagata, Iwamoto & Kasagi 2002; Hasegawa & Kasagi 2011):

$$\begin{aligned} C_f &= \frac{6}{Re} + 3\int_{-1}^{1} y\overline{u'v'}\, \mathrm{d}y \\ &= \frac{6}{Re} + 3\int_{-1}^{1} y\overline{\tilde{u}\tilde{v}}\, \mathrm{d}y + 3\int_{-1}^{1} y\overline{u''v''}\, \mathrm{d}y\, \mathrm{d}t, \end{aligned} \tag{4.5}$$

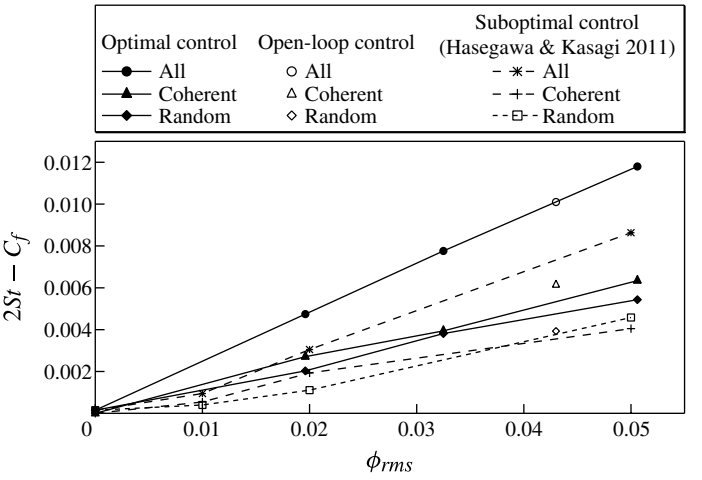

FIGURE 12. Contributions from coherent and random fluctuations to dissimilarity $2St - C_f$.

$$2St = \frac{6}{Re} + 3\int_{-1}^{1} y\overline{\theta' v'}\,\mathrm{d}y$$
$$= \frac{6}{Re} + 3\int_{-1}^{1} y\overline{\tilde{\theta}\tilde{v}}\,\mathrm{d}y + 3\int_{-1}^{1} y\overline{\theta'' v''}\,\mathrm{d}y. \tag{4.6}$$

In the above two equations, the first term on the right-hand side represents the laminar contribution and is constant once the Reynolds number is fixed, whereas the second and third terms correspond to the turbulence contributions. It is evident that the dissimilarity between the Reynolds shear stress and the turbulent heat flux is necessary to achieve dissimilar heat transfer enhancement, i.e. $2St - C_f > 0$. We confirm that C_f and St calculated from the above relationships agree quite well with those obtained from DNS within a error of less than 1 % in all cases. This fact again supports that the velocity and thermal fields reach a fully developed state.

According to (4.5) and (4.6), the difference between $2St$ and C_f can be related to the difference in the weighted turbulent heat flux and Reynolds shear stress as

$$2St - C_f = 3\left\{\int_{-1}^{1} y\left(\overline{\tilde{\theta}\tilde{v} - \tilde{u}\tilde{v}}\right)\,\mathrm{d}y + \int_{-1}^{1} y\left(\overline{\theta'' v'' - u'' v''}\right)\,\mathrm{d}y\right\}. \tag{4.7}$$

The first and second terms on the right correspond to the contributions from the coherent and random fluctuations, respectively. They are plotted as a function of ϕ_{rms} in figure 12. In the optimal control, the contributions of coherent and random components are almost identical regardless of ϕ_{rms}. This trend is similar to that observed in the suboptimal control (Hasegawa & Kasagi 2011). However, both the coherent and random contributions are very much enhanced in the present optimal control, and therefore higher dissimilarity is achieved. In the open-loop control, the coherent contribution is almost the same as that in the optimal control at $\phi_{rms} = 0.05$, whilst the random contribution is suppressed, so that the overall control performance deteriorates.

In order to clarify the spatial distributions of the coherent and random contributions, the integrands of the coherent and random contributions in (4.7), i.e. $y(\overline{\tilde{\theta}\tilde{v} - \tilde{u}\tilde{v}})$

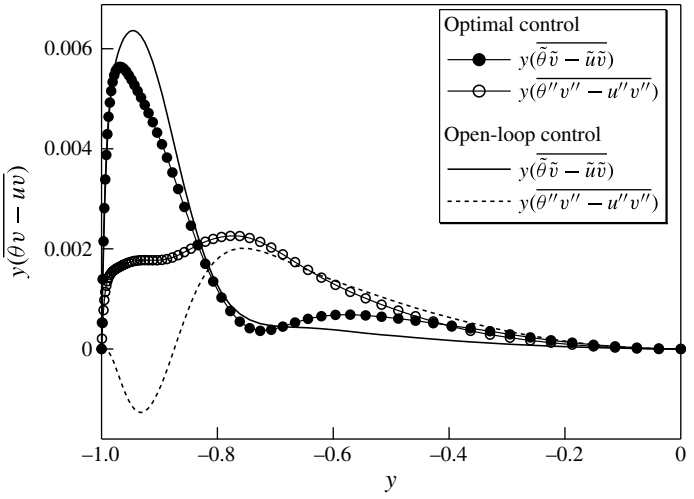

FIGURE 13. The difference in the weighted turbulent heat flux and Reynolds shear stress arising from coherent and random fluctuations.

and $y(\overline{\theta''v'' - u''v''})$, in the optimal control of case 1 and the open-loop control are plotted as a function of y in figure 13. The coherent contribution has a prominent peak near the wall and most of the contribution occurs within $0.75 < |y| < 1.0$, whereas the contribution away from the wall remains small. Good agreement between the coherent contributions in the optimal and open-loop controls implies that the presence or absence of the random input has a minor effect on the coherent velocity and thermal fields.

In contrast, the random contribution in the optimal control is distributed more evenly throughout the channel. The profiles in the optimal and open-loop controls agree well away from the wall. Approaching to the wall, however, the random contribution of the open-loop control is rapidly suppressed and eventually changes its sign close to the wall, i.e. $|y| > 0.9$. This could be attributed to the absence of the random control input, and is consistent with the smaller random contribution shown in figure 12.

Considering the fact that the single sinusoidal wave of $(k_x, k_z) = (3.2, 0)$ is dominant in the present control input, it is rather surprising that the random contribution is generally comparable with the coherent one. In particular, the significant random contribution is maintained even in the open-loop control, where only the single sinusoidal travelling wave is applied. This suggests that the travelling wave input causes dissimilarity through not only the direct modification of the coherent field, but also indirect effects on the random turbulent field. In §§ 4.3 and 4.4, we investigate the mechanisms of dissimilarity in the coherent and random fields, respectively.

4.3. *Dissimilarity in the coherent field*

The phase average of the velocity and thermal fields is shown in figure 14. Note that the corresponding control input at the bottom wall is shown in figure 11. It is found that the distributions of $\langle u \rangle$ and $\langle \theta \rangle$ are very different (see figure 14*a,b*). The iso-lines of $\langle u \rangle$ are almost parallel near the wall, whereas the signature of wall blowing/suction is clearly observed in the distribution of $\langle \theta \rangle$. This essential difference is caused by

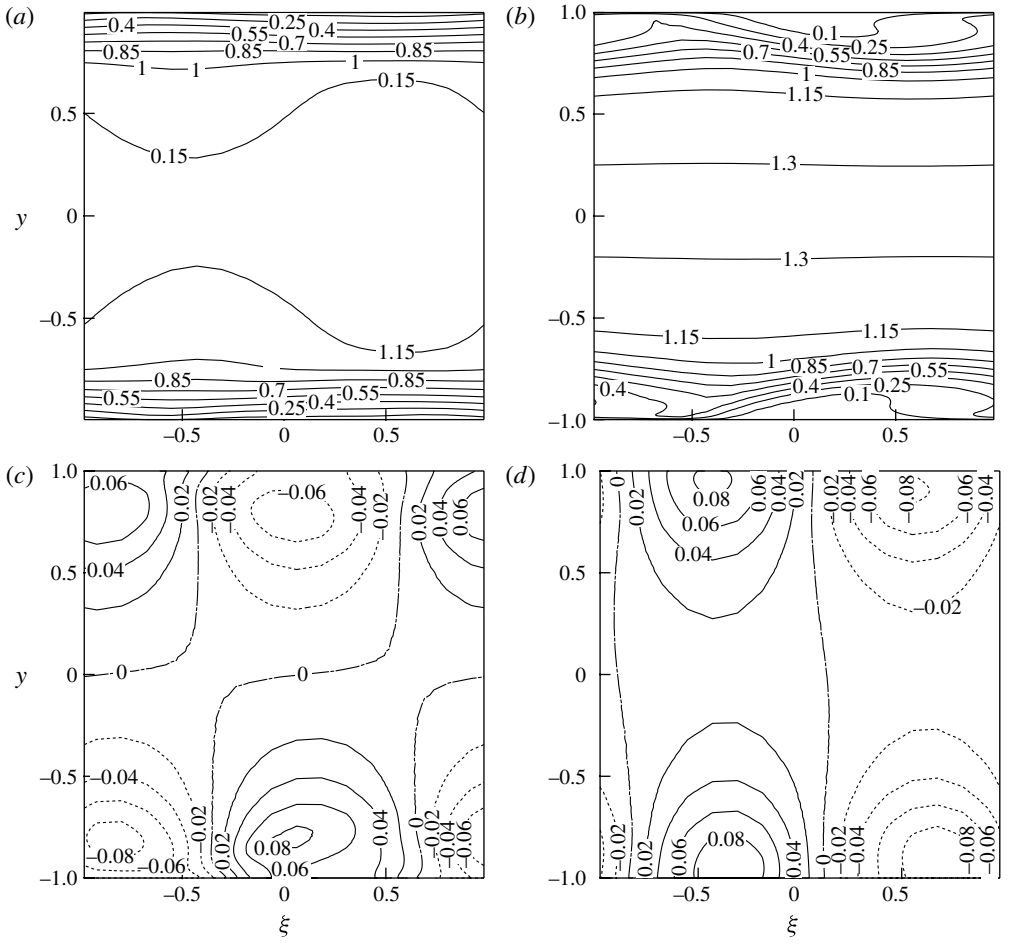

FIGURE 14. Conditionally averaged quantities: (*a*) $\langle u \rangle$, (*b*) $\langle \theta \rangle$, (*c*) $\langle v \rangle$ and (*d*) $\langle p \rangle$.

the coherent pressure fluctuation induced by the wall blowing/suction (see figure 14*c,d* for $\langle v \rangle$ and $\langle p \rangle$, respectively). The positive and negative pressure regions are generated upstream and downstream of the blowing region. (Note that $\xi = 0$ corresponds to the location where the wall blowing is maximum.) They induce a favourable pressure gradient over the blowing region that accelerates $\langle u \rangle$ so as to compensate the low momentum convected from the near-wall region. Considering the fact that the pressure field instantaneously responds to the control input in an incompressible fluid so that the velocity field satisfies continuity, the lower sensitivity of $\langle u \rangle$ in comparison to $\langle \theta \rangle$ is attributed to the continuity constraint on the velocity vector.

The above difference between the responses of $\tilde{u}$ and $\tilde{\theta}$ to the travelling wave of wall blowing and suction significantly affects the coherent contribution to $2St - C_f$, i.e. $y(\tilde{\theta}\tilde{v} - \tilde{u}\tilde{v})$, as shown in figure 15. The positive peak of $y(\tilde{\theta}\tilde{v} - \tilde{u}\tilde{v})$ occurs above the location of wall blowing, and it exceeds the negative contribution above the suction region. Consequently, the prominent peak of the coherent contribution occurs in the near-wall region as shown in figure 13.

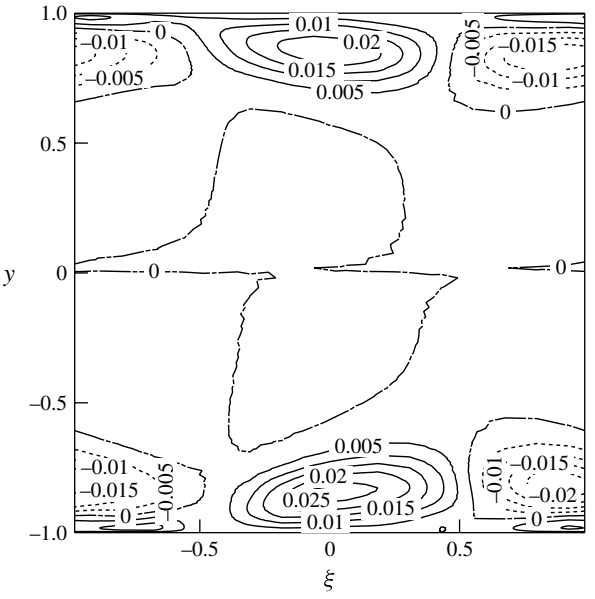

FIGURE 15. Contribution of coherent fluctuation to $2St - C_f$, i.e. $y(\tilde{\theta}\tilde{v} - \tilde{u}\tilde{v})$.

4.4. *Dissimilarity in the random field*

In order to investigate the mechanism of dissimilarity in the random fields, we introduce the eddy viscosity E_v and the eddy diffusivity E_c for heat:

$$E_v = \frac{-\overline{u''v''}}{\left(\dfrac{\mathrm{d}\overline{u}}{\mathrm{d}y}\right)}, \quad E_c = \frac{-\overline{\theta''v''}}{\left(\dfrac{\mathrm{d}\overline{\theta}}{\mathrm{d}y}\right)}. \tag{4.8}$$

As a result, the difference between $\overline{\theta''v''}$ and $\overline{u''v''}$ is expressed by

$$\overline{\theta''v''} - \overline{u''v''} = (Pr_t^{-1}S - 1)\overline{u''v''}. \tag{4.9}$$

Here, S is the ratio of the mean temperature gradient and the mean velocity gradient, i.e. $S = (\mathrm{d}\overline{\theta}/\mathrm{d}y)/(\mathrm{d}\overline{u}/\mathrm{d}y)$. The turbulent Prandtl number is defined as $Pr_t = E_v/E_c$. Equation (4.9) indicates that the dissimilarity between $\overline{\theta''v''}$ and $\overline{u''v''}$ is caused by enhancement of either Pr_t^{-1} or S. The profiles of Pr_t^{-1} and S for the optimal and open-loop controls are plotted in figure 16. The dotted line corresponds to $Pr_t^{-1} = S = 1.0$. It is found that Pr_t^{-1} is dominant only in the near-wall region, i.e. $|y| > 0.8$, whereas S is kept larger than unity away from the wall, i.e. $|y| < 0.8$, being distributed more evenly in the central region of the channel. This indicates that there exist two distinct mechanisms for the dissimilarity in the random field. Interestingly, the prominent peak of Pr_t^{-1} is not observed in the open-loop control, while S is kept larger than unity away from the wall in both the controls. The difference between Pr_t^{-1} in the optimal and open-loop controls explains the significant suppression of the random contribution to the dissimilarity in the near-wall region of $|y| > 0.8$ as shown in figure 13.

Considering that the only difference between the optimal and open-loop controls is the presence or absence of the random component in the control input, we can conclude that the apparent peak of Pr_t^{-1} observed only in the optimal control is caused

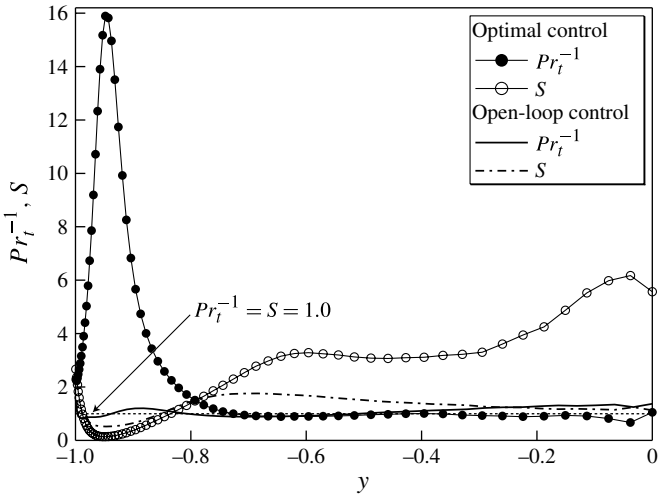

FIGURE 16. Distributions of Pr_t^{-1} and S in the optimal and open-loop controls .

by the random control input through modification of turbulent transport mechanisms near the wall. Consequently, the optimal control achieves higher control performance than the open-loop control as summarized in figure 12.

In contrast, the enhancement of S away from the wall is commonly observed in both the optimal and open-loop controls. As discussed in Hasegawa & Kasagi (2011), this can be considered as the indirect effect of the travelling wave input on the random field. As already shown in figures 14 and 15, the travelling wave of wall blowing and suction significantly affects the coherent velocity and thermal fields. This causes the dissimilarity between the mean velocity and temperature profiles, and therefore indirectly affects the random field through S. The present results indicate that the optimal travelling wave of wall blowing and suction is determined so as to maximize the overall contribution to dissimilarity from the direct and indirect effects on the coherent and random fields, respectively.

5. Scaling of coherent mode

So far, we have shown that the downstream travelling wave of wall blowing and suction causes significant dissimilarity between momentum and heat transfer. One interesting issue is the scaling of the wavelength and phase velocity of the optimal travelling wave. In order to investigate this issue, we conduct DNS with the optimal control at different amplitudes of the control input (cases 1–3), and also lower and higher Reynolds numbers (cases 4 and 5) than the reference case as listed in table 1.

In all the cases, the resultant optimal control inputs are dominated by a single sinusoidal wave travelling downstream, so that the coherent component of the optimal control input can be easily extracted in accordance with the procedures described in § 4. The wavelength of the dominant sinusoidal mode is found to be around 250 in the friction length scale of the controlled flow regardless of the intensity of the control input and the Reynolds number. Similarly, the phase velocity of the optimal travelling wave is commonly around 30 % of the bulk mean velocity, which corresponds to $U_p^+ \approx 5$ in wall units. The ratio of the r.m.s. value of the coherent component and that of the total control input, and the wavelength and phase velocity of the dominant

Re	ϕ_{rms}	λ^{d+}	$\langle\phi\rangle_{rms}/\phi_{rms}$	$U_p(U_p^+)$	C_f/C_{f0}	St/St_0	A	Case
2284	0.05	256	0.84	0.30 (5.16)	0.76	2.02	2.72	Case1
2284	0.04	255	0.84	0.35 (6.15)	0.75	1.73	2.35	Case1F
2284	0.04	258	0.76	0.32 (5.81)	0.77	1.73	2.29	Case1W
1452	0.17	230	0.85	0.28 (4.53)	0.77	2.99	3.86	Case 4
4980	0.03	266	0.56	0.29 (4.80)	0.90	1.54	1.81	Case 5

TABLE 3. Results of optimal control for $Re = 1452, 2284$ and 4980.

Re	L_x	L_z	(N_x, N_y, N_z)	$(\Delta x, \Delta y, \Delta z)$
1452	2.5π	π	(64, 129, 64)	(12.3, 0.12–3.8, 4.9)
2284	2.5π	π	(128, 129, 128)	(9.2, 0.18–5.7, 3.7)
4980	2.5π	π	(256, 193, 128)	(9.2, 0.25–7.62, 7.4)

TABLE 4. Computational domain size, number of grid points, and grid spacings in the open-loop control.

sinusoidal wave are summarized in table 3. It is observed that A achieved at $Re = 4980$ is smaller than those at lower Re. In the present optimal control, the intensity of the control input is determined implicitly by the value of κ in (2.14), so that it is difficult to fix ϕ_{rms} to a prescribed value. Indeed, ϕ_{rms} at $Re = 4980$ is relatively smaller than those in the other cases. Hence, the lower value of A might be attributed simply to the weaker control input at $Re = 4980$. The Reynolds number effect on the control performance can be discussed more clearly in the following open-loop control case, where the intensity of the control input is exactly fixed at different Re.

As already described in § 2, the optimal control input is determined by taking into account flow dynamics within a finite time horizon T. Although the present optimal control achieves much better control performance than the suboptimal control employing a vanishingly small time horizon, there is no guarantee that the present coherent control input is indeed optimal for an infinitely long time horizon. In order to identify the long-term optimal travelling wave, we conduct a series of computations with an open-loop control where the wavelength of a single sinusoidal mode is systematically changed in the range $5/64\pi < \lambda < 5/2\pi$, whereas the intensity of the control input is kept constant at $\phi_{rms} = 0.043$ and also the phase speed is fixed to $U_p = 0.30$ based on the results of the optimal control. The Reynolds number is changed from 1452 to 4980 in accordance with those considered in the optimal control.

In the open-loop control, we employ a finer grid system than that used in the optimal control. The number of grids points, grid spacing and domain size employed in the open-loop control are listed in table 4. In order to obtain reliable C_f and St, the grid systems employed in the open-loop control are finer than those used in cases 1 and 5 for the optimal control at $Re = 2284$ and 4980, respectively. We also note that computations with a spectral method are also conducted for typical cases and good agreement in C_f and St is confirmed between the present and spectral computations.

In figure 17, the obtained C_f and St are plotted as a function of λ. It is found that both C_f and $2St$ are enhanced with increasing λ and their Reynolds number

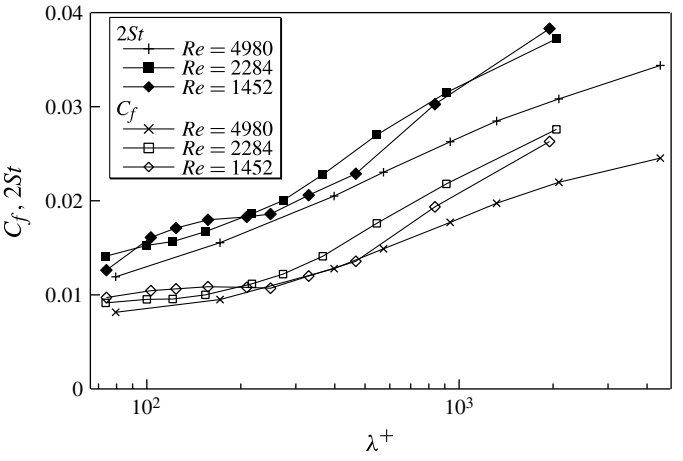

FIGURE 17. C_f, St in the open-loop control with systematically changing the wavelength λ.

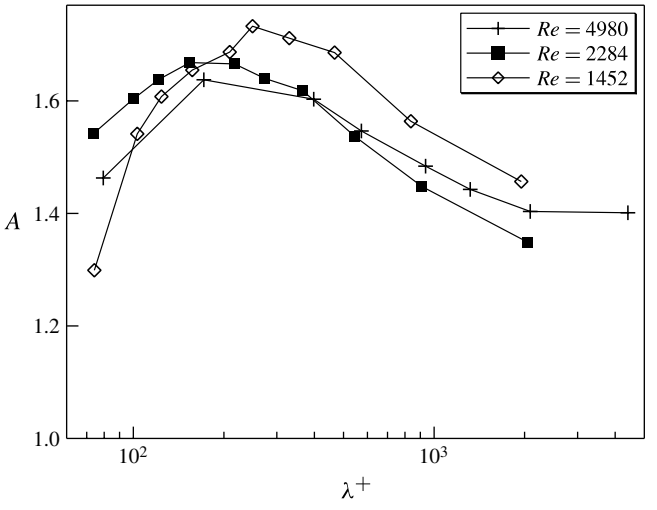

FIGURE 18. A with a single travelling wave.

dependence is not significant. $2St$ is usually larger than C_f, so that the dissimilar heat transfer enhancement is achieved. The resultant A is shown in figure 18. It is found that the maximum value of $A \approx 1.7$ is achieved around $\lambda^+ = 200$–250. This shows good agreement with the wavelength of the dominant sinusoidal mode extracted from the optimal control input listed in table 3. From these results, we can conclude that the present optimization strategy, in spite of its limited time horizon, provides a good estimate of the long-term optimal coherent input, and the downstream travelling wave of wall blowing and suction is a robust and universal control strategy for achieving dissimilar heat transfer enhancement.

6. Conclusions

The spatio-temporal distribution of zero-net-mass-flux wall blowing and suction is determined based on optimal control theory for achieving dissimilar heat transfer

enhancement in a fully developed channel flow at low Reynolds numbers. Although various different thermal conditions are possible in real applications, we consider an ideal system where the averaged momentum and heat transport equations are identical in order to focus on the dissimilarity caused by the continuity constraint on the velocity field. As a result, sustained skin-friction drag reduction and heat transfer augmentation are simultaneously achieved for the first time. More specifically, the skin-friction drag is decreased by 24 %, while the heat transfer is enhanced to more than twice the uncontrolled value when the r.m.s. value of the control input is 5 % of the bulk mean velocity. Consequently, the analogy factor is increased to as high as $A = 2.7$, which is much larger than $A = 1.5$ achieved by the suboptimal control (Hasegawa & Kasagi 2011) at the same intensity of the control input, i.e. $\phi_{rms} = 0.05$.

Surprisingly, the optimal control input is characterized by the superposition of a dominant downstream travelling sinusoidal wave and weaker random fluctuations. Following this result, the optimal control input is decomposed into coherent and random components in order to clarify their mechanisms and quantitative contributions to dissimilar heat transfer enhancement. It is found that the coherent component of the control input causes dissimilarity through direct modification of the coherent velocity and thermal fields. This changes the ratio of the mean velocity and temperature gradients, and therefore indirectly affects the random field as well. Hence, the optimal coherent travelling wave is determined so as to maxmize the sum of these two effects. Meanwhile, the random component of the control input contributes to dissimilarity by changing the turbulent Prandtl number near the wall.

The coherent travelling wave extracted from the optimal control input is of particular importance from the practical viewpoint, since it allows us to achieve dissimilar heat transfer enhancement with a simple open-loop control strategy requiring no information on an instantaneous flow state. Through a series of optimizations at different intensities of the control input and also different Reynolds numbers, it is revealed that the wavelength of the coherent travelling wave is commonly around 250 in the friction length scale, whereas its phase velocity is 30 % of the bulk mean velocity. The Reynolds number effect on the control performance is found to be rather minor within the range of Re considered in the present study. However, further research is necessary to clarify this issue at higher Reynolds numbers.

In practice, the optimal control theory has to be applied within a finite time horizon due to the limitations of computational resources, and therefore the resultant control input is not necessarily long-term optimal. However, the present study shows that the features of the control input optimized within a finite time horizon agree well with those of the long-term optimal travelling wave. Although we have no clear reason for this agreement, one possible explanation could be as follows: the travelling wave is regarded to be steady when the reference frame moves with the phase speed, and therefore so are the induced coherent velocity and thermal fields. Although the time horizon for optimization is not long enough to cover an entire lifetime of near-wall turbulent dynamics, the repeating advancement of the time horizon would successively optimize the coherent travelling wave so as to achieve higher dissimilarity in the induced coherent velocity and thermal fields. Indeed, a qualitatively similar travelling wave was also obtained in the suboptimal control (Hasegawa & Kasagi 2011), where the vanishing small time horizon is employed, although the resultant control performance is not as high as that achieved in the present optimal control.

Recently, various types of travelling-wave-like control input such as wall blowing and suction (Min *et al.* 2006), spanwise wall forcing (Quadrio, Ricco & Viotti 2009) and wall deformation (Nakanishi, Mamori & Fukagata 2012) have been proposed

for skin-friction drag reduction. These control modes with periodic coherence have been developed based on the investigators' subjective insight into the flow physics, and huge computational cost is required to seek the optimal design parameters such as wave amplitude, wavelength and phase velocity. To the best of our knowledge, the present study is the first example where an efficient open-loop control strategy has been derived from optimal control theory. When the optimal control is applied to turbulent flow in the original framework developed in Bewley *et al.* (2001), the optimal control input is generally specific to the instantaneous flow field, so that it does not always contain a coherent component. In order for the optimal control input to have spatio-temporal coherence, it would be necessary to contrive ways to limit the degree of freedom of the control input. Some simple methods, where the cost of control is changed depending on the wavenumber, are proposed in Bewley *et al.* (2001), but they remain to be validated.

While the present study focuses on an ideal situation, the properties of the optimal travelling wave should generally depend on flow and thermal conditions: the varicose mode of wall blowing and suction may not work in open flows. The streamwise development of velocity and thermal fields has to be taken into account near the inlet of a heat exchanger. The buoyancy effects neglected in the present study play important roles in flows with non-marginal temperature difference. The Prandtl number of the working fluid is not always close to unity in practice. For instance, the Prandtl number of water is around 7 under standard conditions, whereas engine oils have much larger values ranging from 10^2 to 10^4. It is of great interest to clarify how different flow and thermal conditions affect the properties of the optimal control mode.

Although the present open-loop control significantly simplifies the original optimal control, it is highly desirable to achieve a similar control performance with passive means with a view to practical application. Optimal theory has been successfully applied to the shape optimization of a solid–fluid interface for dissimilar heat transfer enhancement in steady laminar flow (Morimoto, Suzuki & Kasagi 2010), while its application to unsteady turbulent flows remains to be done in future work.

The present study focuses on maximizing the analogy factor, which has often been used for evaluating the performance of heat exchangers. However, the thermodynamical analysis of entropy generation in heat transfer processes indicates that the relative cost and merit of pressure drop and heat transfer should be different in each application (see e.g. Bejan 1978). Accordingly, a general form of a cost function may be given by a weighted sum of C_f and St with different weighting coefficients as considered in Hasegawa & Kasagi (2011). A similar discussion for drag reduction control alone has been made in Frohnapfel, Hasegawa & Quadrio (2012), where the optimization problem is formulated as a compromise between energy consumption and convenience. It would be interesting to extend such an approach to seek a compromise point between the heat transfer and the pressure drop.

Acknowledgements

The authors are grateful to Professor Y. Suzuki and Professor N. Shikazono at the University of Tokyo for fruitful discussions during the course of the present work. This work is supported by the Ministry of Education, Culture, Sports, Science and Technology of Japan (MEXT) through the Grant-in-Aid for Young Scientists (B) (No. 23760176) and the Grant-in-Aid for Scientific Research (B) (No. 25289037). Y.H. gratefully acknowledges the support from the Japan Society for the Promotion of Science (JSPS) Postdoctoral Fellowship for Research Abroad.

Case	C_f	$C_{f\,net}$	$C_{f\,csv}$	A	A_{net}	A_{csv}
Case 1	6.90×10^{-3}	4.50×10^{-3}	8.73×10^{-3}	2.72	4.17	2.15
Case 2	6.87×10^{-3}	5.62×10^{-3}	7.65×10^{-3}	2.12	2.59	1.90
Case 3	6.99×10^{-3}	6.32×10^{-3}	7.28×10^{-3}	1.68	1.86	1.61

TABLE 5. Control performance taking into account power consumption of actuators.

Appendix A. Heat transfer enhancement per unit total power input

As discussed in Hasegawa & Kasagi (2011), the ideal power consumption P_c^* of zero-net-mass-flux wall blowing/suction is given by

$$P_c^* = \overline{p^{*\prime}\phi^{*\prime} + \tfrac{1}{2}\rho^*\phi^{*\prime 3}}. \tag{A 1}$$

Hence, we introduce the equivalent wall friction $(\tau_w)_{net}$ based on the total power consumption as

$$(\tau_w^*)_{net} = \frac{P_p^* + P_c^*}{u_b^*} = \tau_w^* + \frac{1}{u_b^*}\overline{\left(p^{*\prime}\phi^{*\prime} + \tfrac{1}{2}\rho^*\phi^{*\prime 3}\right)}, \tag{A 2}$$

where P_p^* is the pumping power. By using $(\tau_w)_{net}$, the friction coefficient is defined as $C_{f_{net}} = (\tau_w)_{net}/(\rho^* U_b^{*2}/2)$. Accordingly, the analogy factor is also defined as $A_{net} = 2St/C_{f_{net}}$, which represents heat transfer per unit total power consumption.

It is known that travelling-wave-like wall blowing/suction often causes negative power consumption (see e.g. Hasegawa & Kasagi 2011). Since energy recovery from the flow system is unrealistic, we also introduce a more conservative estimate of P_c so as to count only positive power consumption at each actuator location, as

$$\left(P_c^*\right)_{csv} = \overline{S_1 p^{*\prime}\phi^{*\prime} + \tfrac{1}{2}S_2\rho^*\phi^{*\prime 3}}, \tag{A 3}$$

where S_1 and S_2 are switching coefficients defined as

$$S_1 = \begin{cases} 1 & (p^{*\prime}\phi^{*\prime} > 0) \\ 0 & (p^{*\prime}\phi^{*\prime} < 0), \end{cases} \quad S_2 = \begin{cases} 1 & (\phi^{*\prime} > 0) \\ 0 & (\phi^{*\prime} < 0). \end{cases} \tag{A 4}$$

A equivalent wall friction based on $(P_c^*)_{csv}$ is given by $(\tau_w^*)_{csv} = \{P_p^* + (P_c^*)_{csv}\}/u_b^*$, so that the corresponding analogy factor is defined as $A_{csv} = 2St/C_{f_{csv}}$, where $C_{f_{csv}} = (\tau_w)_{csv}/(\rho^* U_b^{*2}/2)$.

In table 5, the control performances taking into account actuator power consumption are summarized for cases 1–3. It is found that $C_{f_{net}}$ is smaller than C_f. This indicates that the net power consumption of the actuator is negative. As a result, A_{net} becomes larger than A. When energy recovery from the flow is not allowed, $C_{f_{csv}}$ is larger than C_f by definition, and therefore A_{csv} is reduced. However, A_{csv} remains larger than unity even in such a conservative evaluation.

Appendix B. Effects of the form of the cost functional on the control performance

Since the time horizon employed in optimal control theory always remains finite due to computational costs, a control input optimized under a cost function directly

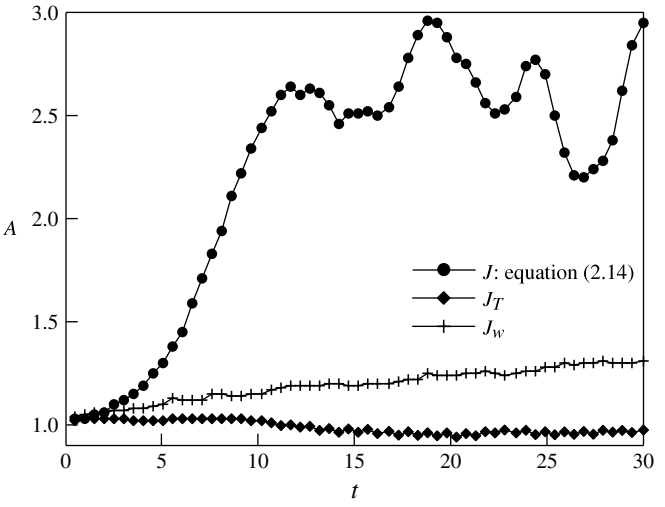

FIGURE 19. Time trace of analogy factor A obtained by different cost functionals.

including an objective quantity is not necessarily long-term optimal. Indeed, Bewley *et al.* (2001) reported that including the terminal kinetic energy in the cost functional is more effective in drag reduction than including the drag itself. Hence, we tested several different types of a cost functional in addition to (2.14).

First, we consider a cost functional including the terminal value of A instead of the time integral of A within a time horizon, namely,

$$J_T = \kappa \int_0^T \int_{\Gamma_{2\pm}} \frac{1}{2}\phi^2 \,\mathrm{d}S\,\mathrm{d}t - A\,(T)\,T, \tag{B 1}$$

where κ is a constant presenting the relative cost of the control input.

Considering that the dissimilarity between the weighted Reynolds shear stress and heat flux is the direct cause of enhancement of A as shown in (4.7), another option is to implement them in the cost functional as

$$J_W = \kappa \int_0^T \int_{\Gamma_{2\pm}} \frac{1}{2}\phi^2 \,\mathrm{d}S\,\mathrm{d}t - 3\int_0^T \int_{-1}^{1} y\left(\overline{\theta' v' - u' v'}\right)\,\mathrm{d}y\,\mathrm{d}t. \tag{B 2}$$

The control results obtained under the above two cost functionals (B 1) and (B 2) with $\kappa = 4 \times 10^{-3}$ and 9×10^{-3} respectively are compared with that obtained under the cost functional (2.14) in figure 19. The values of κ are decided so as to make the r.m.s. value of the control input similar in all the cases. It is found that the cost functional (2.14) achieves highest A among those tested. Although various other types of cost functional are possible in principle, there exists no systematic way to find a better form. Examining other types of the cost functional remains for future work.

REFERENCES

ABERGEL, F. & TEMAM, R. 1990 On some control problems in fluid mechanics. *Theor. Comput. Fluid Dyn.* **1**, 303–325.

ANTONIA, R. A. & KRISHNAMOORTHY, L. V. 1988 Correlation between the longitudinal velocity fluctuation and temperature fluctuation in the near-wall region of a turbulent boundary layer. *Intl J. Heat Mass Transfer* **31**, 723–730.

BEJAN, A. E. 1978 General criterion for rating heat-exchanger performance. *Intl J. Heat Mass Transfer* **21**, 655–658.

BEWLEY, T., MOIN, P. & TEMAM, R. 2001 DNS-based predictive control of turbulence: an optimal benchmark for feedback algorithms. *J. Fluid Mech.* **447**, 179–225.

CHOI, H., MOIN, P. & KIM, J. 1994 Active turbulence control for drag reduction in wall-bounded flows. *J. Fluid Mech.* **262**, 75–110.

EIAMSA-ARD, S. & PROMVONGE, P. 2011 Influence of double-sided delta-wing tape insert with alternate-axes on flow and heat transfer characteristics in a heat exchanger tube. *Chin. J. Chem. Engng* **19** (3), 410–423.

FROHNAPFEL, B., HASEGAWA, Y. & KASAGI, N. 2010 Friction drag reduction through damping of the near-wall spanwise velocity fluctuation. *Intl J. Heat Fluid Flow* **31**, 434–441.

FROHNAPFEL, B., HASEGAWA, Y. & QUADRIO, M. 2012 Money versus time: evaluation of flow control in terms of energy consumption and convenience. *J. Fluid Mech.* **700**, 406–418.

FUKAGATA, K., IWAMOTO, K. & KASAGI, N. 2002 Contribution of Reynolds stress distribution to the skin friction in wall-bounded flows. *Phys. Fluids* **14**, L73–L76.

HASEGAWA, Y. & KASAGI, N. 2011 Dissimilar control of momentum and heat transfer in a fully developed turbulent channel flow. *J. Fluid Mech.* **683**, 57–93.

IIDA, O. & KASAGI, N. 1997 Direct numerical simulation of unstably stratified turbulent channel flow. *Trans. ASME: J. Heat Transfer* **119**, 53–61.

IIDA, O., KASAGI, N. & NAGANO, Y. 2002 Direct numerical simulation of turbulent channel flow under stable density stratification. *Intl J. Heat Mass Transfer* **45**, 1693–1703.

KASAGI, N., HASEGAWA, Y., FUKAGATA, K. & IWAMOTO, K. 2012 Control of turbulent transport: Less friction and more heat transfer. *Trans. ASME: J. Heat Transfer* **134**, 031009.

KASAGI, N., KURODA, A. & TOMITA, Y. 1992 Direct numerical simulation of passive scalar field in a turbulent channel flow. *Trans. ASME: J. Heat Transfer* **114**, 598–606.

KEYS, W., CRAWFORD, M. E. & WEIGAND, B. 2005 *Convective Heat and Mass Transfer*, 4th edn. McGraw-Hill.

KIM, J., MOIN, P. & MOSER, R. 1987 Turbulence statistics in fully developed channel flow at low Reynolds number. *J. Fluid Mech.* **177**, 133–166.

LEE, C., KIM, J. & CHOI, H. 1998 Suboptimal control of turbulent channel flow for drag reduction. *J. Fluid Mech.* **358**, 245–258.

MANGLIK, R. M. & BERGLES, A. E. 1995 Heat transfer and pressure drop correlations for the rectangular offset strip fin compact heat exchanger. *Exp. Therm. Fluid Sci.* **10**, 171–180.

MIN, T., KANG, S. M., SPEYER, J. L. & KIM, J. 2006 Sustained sub-laminar drag in a fully developed channel flow. *J. Fluid Mech.* **558**, 309–318.

MORIMOTO, K., SUZUKI, Y. & KASAGI, N. 2010 Optimal shoe design of compact heat exchangers based on adjoint analysis of momentum and heat transfer. *J. Therm. Sci. Tech.* **5**, 24–35.

NAGANO, Y., HATTORI, H. & HOURA, T. 2004 DNS of velocity and thermal fields in turbulent channel flow with transverse-rib roughness. *Intl J. Heat Fluid Flow* **25**, 393–403.

NAKANISHI, R., MAMORI, H. & FUKAGATA, K. 2012 Relaminarization of turbulent channel flow using travelling wave-like wall deformation. *Intl J. Heat Fluid Flow* **35**, 152–159.

QUADRIO, M., RICCO, P. & VIOTTI, C. 2009 Streamwise-travelling waves of spanwise wall velocity for turbulent drag reduction. *J. Fluid Mech.* **627**, 161–178.

RAI, M. & MOIN, K. 1991 Direct simulations of turbulent flow using finite-difference scheme. *J. Comput. Phys.* **96**, 15–53.

REYNOLDS, O. 1874 On the extent and action of the heating surface of steam boilers. *Manchester Lit. Phil. Soc. Mem. Proc.* **14**, 7–12.

SATAKE, S. & KASAGI, N. 1996 Turbulence control with wall-adjacent thin layer damping spanwise velocity fluctuations. *Intl J. Heat Fluid Flow* **17**, 343–352.

SPALART, P., MOSER, R. & ROGERS, M. 1991 Spectral methods for the Navier–Stokes equations with one infinite and two periodic directions. *J. Comput. Phys.* **96**, 297–324.

STASIEK, J., COLLINS, M. W., CIOFALO, M. & CHEW, P. E. 1996 Investigation of flow and heat transfer in corrugated passages – l. Experimental results. *Intl J. Heat Mass Transfer* **39**, 149–164.